Available online at www.sciencedirect.com
ScienceDirect
Comput. Methods Appl. Mech. Engrg. 400 (2022) 115543
Computer methods in applied mechanics and engineering
www.elsevier.com/locate/cma

A unified non-linear energy dissipation-based plastic-damage model for cyclic loading

A. Cornejo[a,b,*], S. Jiménez[a,b], L.G. Barbu[a,b], S. Oller[a,c], E. Oñate[a,b]

[a] *Centre Internacional de Mètodes Numèrics en Enginyeria (CIMNE), Campus Norte UPC, 08034 Barcelona, Spain*
[b] *Universidad Politécnica de Cataluña (UPC), Campus Norte UPC, 08034 Barcelona, Spain*
[c] *Consejo Nacional y de Investigaciones Científicas y Técnicas (CONICET), Facultad de Ingeniería, Universidad Nacional de Salta, Av. Bolivia 5150, 4400, Salta, Argentina*

Received 13 May 2021; received in revised form 19 June 2022; accepted 11 August 2022
Available online 30 August 2022

Abstract

A new energy-dissipation-based rate-independent constitutive law within the framework of elastoplasticity coupled with damage is proposed. With this methodology, the inelastic strains and the stiffness degradation exhibited by quasi-brittle materials under monotonic or cyclic loading conditions are taken into account. The proposed constitutive model is able to capture micro-cracks closure-reopening effects due to load reversal. A wide variety of hardening/softening laws on the stress–strain relationship are described and considered for the novel normalized plastic-damage energy dissipation internal variable. This normalized internal variable allows the model to be independent on the sign of the load and dissipate different fracture energies (tensile, compressive and potentially shear) in a natural way. Several numerical examples are presented in order to ensure the efficiency and validity of the proposed model for simulating the non-linear behaviour of quasi-brittle materials under monotonic and cyclic loading. Some numerical aspects of the implemented algorithm and the return mapping procedure are also described in detail and discussed.

Keywords: Fracture mechanics; Plasticity; Constitutive modelling; Cyclic loading; Damage; Crack closure-reopening

1. Introduction

One of the most relevant or crucial aspects when studying the failure analysis of structures is the modelling of the crack onset and propagation. Some materials, when submitted to an increasing loading, exhibit distributed and localized degradation of their physical properties. The phenomenological response of the material is characterized by a linear ascending curve (elastic branch) followed by a change in strength (post peak regime). In tension, a softening post peak curve is usually expected whereas an exponential hardening is commonly seen in compressive experiments, especially of concrete materials. When the material is unloaded after reaching the post-peak load, non-recoverable (plastic) strains and a stiffness degradation (damage) is generally observed in experiments (Fig. 1).

The *damage* or stiffness degradation of the material is generally assumed to be due to the growth and coalescence of voids and micro-cracks within the material at the interface between cement paste and aggregates in the case

* Corresponding author at: Universidad Politécnica de Cataluña (UPC), Campus Norte UPC, 08034 Barcelona, Spain.
E-mail address: acornejo@cimne.upc.edu (A. Cornejo).

https://doi.org/10.1016/j.cma.2022.115543

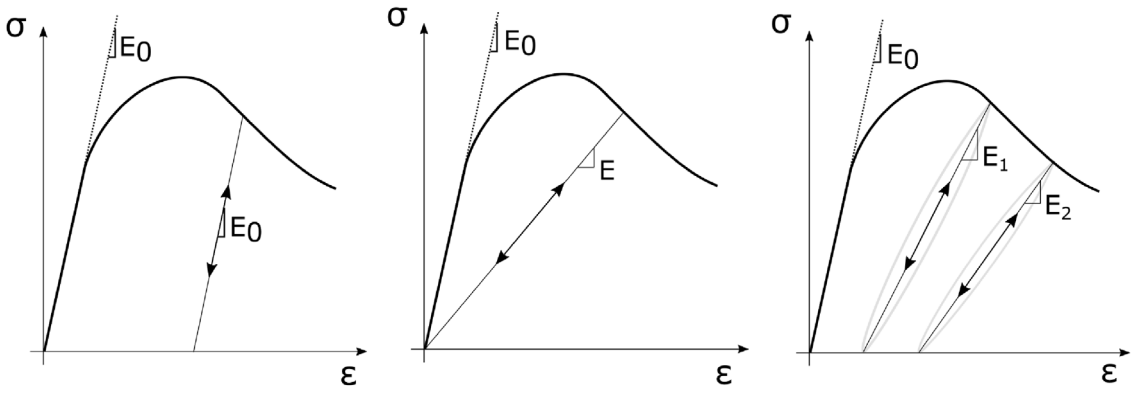

(a) Plastic behaviour (b) Damage behaviour (c) Real coupled behaviour

Fig. 1. Different material mechanical behaviours.

of concrete. When unloading, this aforementioned deterioration of the material and the growth of micro-defects prevents the complete re-closing of cracks, which leads to the development of plastic strains. This implies that a general quasi-brittle material phenomenologically behaves as depicted in Fig. 1(c), exhibiting stiffness degradation and developing non-recoverable plastic strains. If the load is totally reversed, i.e. the former tensile stresses are now in a compressive state, a re-closing effect of the crack or stress-recovery can be expected [1].

As stated before, damage mechanics is mainly related to a stiffness loss due to a micro-cracks growth. There are many works in literature that exploit these ideas and the concept of effective stresses [2–8] as well as models that combine the damage effect with non-recoverable strain development [9–15]. Several authors have proposed an anisotropic damage model [13,14,16,17] taking advantage of the principle of maximum dissipation for defining mathematically the increment of the compliance tensor (reduction of the constitutive elastic tensor), which serves as a basis of the present work. Additionally, in order to capture the crack opening re-closure effect, a tensile/compressive split of the compliance tensor is proposed.

The objective of this work is to extend the coupled plastic-damage model proposed by Meschke et al. [13] and Wu and Cervera [14] for cyclic loading to be able to capture stress-recovery effects [1] using a novel internal variable: the normalized plastic-damage energy dissipation [18–21]. This approach allows the use of equal hardening curves in tension and compression with no added operations, even though different fracture energies can be used. The hardening laws employed are formulated according to the new internal variable. This ensures a stable, energy-conservative and efficient plastic damage model. The new internal variable measures the energy dissipation performed by the damage and plastic processes and it is normalized it by the total fracture energy available. In order to take into account different tensile and compressive fracture energies, an averaging is performed depending on the current stress-state.

The extension of the plastic-damage constitutive model affects the hardening laws in such a way that requires the mathematical derivation of the plastic consistency factor and the tangent constitutive matrix, now dependent of the new internal variable.

It is important to note that the plastic behaviour within the plastic-damage model consists in an isotropic plasticity law. This means that Bauschinger effects cannot be modelled but could be included without major modifications. Indeed, only the back stress calculation and its corresponding contribution to the plastic multiplier should be included.

This paper is organized as follows. Section 2 states the coupled plastic-damage model, the internal variables and the return mapping algorithm without including crack re-closure effects for simplicity. Section 3 describes the generalization of the proposed plastic damage model to be able to model crack opening re-closure or stress recovery effects. Section 4 derives the hardening/softening laws based on the energy dissipation. Section 5 shows a collection of numerical examples which results are compared against experimental data and other existing methodologies.

2. Plastic-damage mechanics

Coupled plastic-damage models are widely used for simulating the stiffness degradation and the irrecoverable plastic strain generation exhibited by solid materials. Among the many references in this field we note the work of Lee and Fenves [22,23], Lubliner et al. [12], Meschke et al. [13], Armero and Oller [24], Oller et al. [9,15], Oñate et al. [25], Wu and Cervera [14], Wu et al. [26], Luccioni et al. [10] and Poliotti et al. [11].

In this section, a generalization of the coupled plastic-damage model proposed by Wu and Cervera [14] is described based on plastic-damage model [9,12,24]. This generalization implies that the softening/hardening laws used to describe the stress–strain relationship is based on a new internal variable: the normalized non-linear plastic-damage energy dissipation κ^{pd}. This overcomes the limitations of using a strain measure as an internal variable for the softening process and provides a thermodynamically energy-consistent formulation in a natural way, taking into account different tensile and compressive fracture energies without any additional change. Mesh objectivity is ensured by means of a FE characteristic length normalization of the available fracture energy given to the system [6].

If we restrict the problem to a purely mechanical theory, the second law of the thermodynamics states that the energy dissipation rate $\dot{\mathcal{D}}$ of an admissible deformation process is given by the Clasius–Duhem inequality:

$$\dot{\mathcal{D}} := \boldsymbol{\sigma} : \dot{\boldsymbol{\varepsilon}} - \dot{\psi} \geq 0 \tag{1}$$

where $\boldsymbol{\sigma}$ and $\boldsymbol{\varepsilon}$ are the second order stress and strain tensors, respectively. $\dot{\psi}$ is the Helmholtz free energy density function of the current material.

Following Armero and Oller [24], Oller et al. [9], Wu and Cervera [14], the Helmholtz free energy density function for an elasto-plastic solid with stiffness degradation, assuming infinitesimal strains, can be expressed as:

$$\psi = \frac{1}{2}(\boldsymbol{\varepsilon} - \boldsymbol{\varepsilon}^p) : \mathbf{D} : (\boldsymbol{\varepsilon} - \boldsymbol{\varepsilon}^p) + \psi^p \tag{2}$$

being $\psi^p = \psi^p(\kappa^{pd})$ the potential function that models the inelastic response in terms of a generic internal variable κ^{pd}, $\mathbf{D}$ the secant constitutive tensor and $\boldsymbol{\varepsilon}^p$ the plastic strain tensor. Inserting the temporal derivative of Eq. (2) into Eq. (1) we obtain

$$\left(\boldsymbol{\sigma} - \frac{\partial \psi}{\partial \boldsymbol{\varepsilon}^e}\right) : \dot{\boldsymbol{\varepsilon}} + \boldsymbol{\sigma} : \dot{\boldsymbol{\varepsilon}}^p - \frac{1}{2}\boldsymbol{\varepsilon}^e : \dot{\mathbf{D}} : \boldsymbol{\varepsilon}^e - \frac{\partial \psi^p}{\partial \kappa^{pd}}\dot{\kappa}^{pd} \geq 0. \tag{3}$$

In order to satisfy this inequality for $\forall\, \dot{\boldsymbol{\varepsilon}}$, the following condition must be fulfilled:

$$\boldsymbol{\sigma} - \frac{\partial \psi}{\partial \boldsymbol{\varepsilon}^e} \geq 0 \tag{4}$$

which means that the stress tensor can be retrieved by

$$\boldsymbol{\sigma} = \frac{\partial \psi}{\partial \boldsymbol{\varepsilon}^e} = \mathbf{D} : (\boldsymbol{\varepsilon} - \boldsymbol{\varepsilon}^p). \tag{5}$$

As both the plastic strain and the material stiffness can vary along time, the stress rate $\dot{\boldsymbol{\sigma}}$ is computed as [13,14]

$$\dot{\boldsymbol{\sigma}} = \mathbf{D} : (\dot{\boldsymbol{\varepsilon}} - \dot{\boldsymbol{\varepsilon}}^p) + \dot{\mathbf{D}} : (\boldsymbol{\varepsilon} - \boldsymbol{\varepsilon}^p). \tag{6}$$

By using the identity described in Meschke et al. [13] and Wu and Cervera [14] involving the compliance tensor increment $\dot{\mathbf{D}} = -\mathbf{D} : \dot{\mathbf{C}} : \mathbf{D}$, one can rewrite Eq. (6) as

$$\dot{\boldsymbol{\sigma}} = \mathbf{D} : (\dot{\boldsymbol{\varepsilon}} - \dot{\boldsymbol{\varepsilon}}^p - \dot{\mathbf{C}} : \boldsymbol{\sigma}). \tag{7}$$

Based on the above mathematical expressions, the energy dissipation inequality can be rewritten as

$$\dot{\mathcal{D}} = \frac{1}{2}\boldsymbol{\sigma} : \dot{\mathbf{C}} : \boldsymbol{\sigma} + \boldsymbol{\sigma} : \dot{\boldsymbol{\varepsilon}}^p - \frac{\partial \psi^p}{\partial \kappa^{pd}}\dot{\kappa}^{pd} \geq 0. \tag{8}$$

In order to identify if the material is in elastic or plastic state, it is required to define a failure criterion $\mathcal{F}(\boldsymbol{\sigma}, \kappa^{pd})$ which has to be convex, differentiable and a smooth mathematical function:

$$\mathcal{F}(\boldsymbol{\sigma}, \kappa^{pd}) = f(\boldsymbol{\sigma}) - \mathcal{K}(\kappa^{pd}) \tag{9}$$

where $f(\boldsymbol{\sigma})$ is the uniaxial equivalent stress (either Rankine, Von Mises, Tresca, Drucker–Prager, etc.) and $\mathcal{K}$ is the uniaxial stress threshold, which controls the strength of the material and follows a hardening/softening law depending of an internal variable κ^{pd} defined in the following paragraphs.

Following the classical definition of associative plasticity, the dissipative flow tensor $\boldsymbol{\Lambda} = \frac{\partial \mathcal{F}}{\partial \boldsymbol{\sigma}}$ defines the dissipative plastic strain rate $\dot{\boldsymbol{\varepsilon}}^p$. Additionally, the plastic multiplier increment $\dot{\lambda}$ satisfies the standard Kuhn–Tucker loading/unloading consistency conditions:

$$\dot{\lambda} \geq 0, \quad \mathcal{F}(\boldsymbol{\sigma}, \kappa^{pd}) \leq 0, \quad \mathcal{F}(\boldsymbol{\sigma}, \kappa^{pd})\dot{\lambda} = 0. \tag{10}$$

The plastic-damage distribution of the material response is controlled by a model parameter $\xi \in (0, 1)$ (Wu and Cervera [14]), which defines the behaviour material from fully plastic ($\xi = 0$) to only damage or stiffness degradation ($\xi = 1$). The ξ parameter can be calibrated by considering the stiffness and plastic strains developed in a cyclic experiment. This implies that the plastic strain increment is computed as (Meschke et al. [13], Wu and Cervera [14])

$$\dot{\boldsymbol{\varepsilon}}^p = (1 - \xi)\,\dot{\lambda}\,\frac{\partial \mathcal{F}}{\partial \boldsymbol{\sigma}} = (1 - \xi)\,\dot{\lambda}\,\boldsymbol{\Lambda}. \tag{11}$$

The stiffness degradation induced by the damage is taken into account by means of a compliance tensor rate $\dot{\mathbf{C}}$ which can be obtained via (Meschke et al. [13])

$$\dot{\mathbf{C}} = \xi\,\dot{\lambda}\,\frac{\boldsymbol{\Lambda} \otimes \boldsymbol{\Lambda}}{\boldsymbol{\Lambda} : \boldsymbol{\sigma}}. \tag{12}$$

Note that the compliance matrix $\mathbf{C}$ corresponds to the inverse of the secant constitutive tensor $\mathbf{C} = \mathbf{D}^{-1}$.

When the material is in loading conditions implies that $\dot{\lambda} \geq 0$. In order to obtain the value of $\dot{\lambda}$, one can take advantage of the consistency condition $\dot{\mathcal{F}} = 0$, applying the chain rule as

$$\dot{\mathcal{F}} = \frac{\partial \mathcal{F}}{\partial \boldsymbol{\sigma}} : \dot{\boldsymbol{\sigma}} + \underbrace{\frac{\partial \mathcal{F}}{\partial \mathcal{K}}}_{-1}\,\dot{\mathcal{K}} = 0, \tag{13}$$

The *normalized plastic damage non-linear energy dissipation* κ^{pd} can be computed as

$$\kappa^{pd} = \int_{t=0}^{t=T} \dot{\kappa}^{pd}\,dt \tag{14}$$

where $\dot{\kappa}^{pd}$ is calculated as

$$\dot{\kappa}^{pd} = \frac{1}{g_f}\left(\boldsymbol{\sigma} : \dot{\boldsymbol{\varepsilon}}^p + \frac{1}{2}\boldsymbol{\sigma} : \dot{\mathbf{C}} : \boldsymbol{\sigma}\right) \tag{15}$$

and the volumetric fracture energy $1/g_f = \left(\frac{r}{g_t} + \frac{1-r}{g_c}\right)$ ponderated over the tension and compression fracture energies (g_t and g_c respectively) depending on the r parameter which ranges from 0 (pure compression) to 1 (pure tension). The value of r is computed as:

$$r = \frac{\sum_{i=1}^{3}\langle\sigma_i\rangle}{\sum_{i=1}^{3}|\sigma_i|}\ ,\ \langle\sigma_i\rangle = \frac{1}{2}(\sigma_i + |\sigma_i|) \tag{16}$$

being σ_i the principal stresses.

Eq. (15) shows that there are two energy dissipation mechanisms, one related to the plasticity process ($\boldsymbol{\sigma} : \dot{\boldsymbol{\varepsilon}}^p$) and another one due to the loss of stiffness of the material ($\frac{1}{2}\boldsymbol{\sigma} : \dot{\mathbf{C}} : \boldsymbol{\sigma}$).

Inserting the definition in Eq. (15) into Eq. (13) yields

$$\boldsymbol{\Lambda} : \dot{\boldsymbol{\sigma}} - \dot{\mathcal{K}} = 0 \implies \boldsymbol{\Lambda} : \dot{\boldsymbol{\sigma}} - \frac{\partial \mathcal{K}}{\partial \kappa^{pd}}\,\dot{\kappa}^{pd} = 0. \tag{17}$$

Inserting Eqs. (11) and (12) into the previous expression and rearranging the terms one can estimate the value of the plastic multiplier increment $\dot{\lambda}$ (see Appendix A for more details):

$$\dot{\lambda} = \frac{\boldsymbol{\Lambda} : \mathbf{D} : \dot{\boldsymbol{\varepsilon}}}{A + B + C + D} \tag{18}$$

being

$$A = (1-\xi)\boldsymbol{\Lambda} : \mathbf{D} : \boldsymbol{\Lambda}, \tag{19a}$$

$$B = (1-\xi)\frac{\partial \mathcal{K}}{\partial \kappa^{pd}}\boldsymbol{\sigma} : \boldsymbol{\Lambda}/g_f, \tag{19b}$$

$$C = \xi\,\boldsymbol{\Lambda} : \mathbf{D} : \frac{\boldsymbol{\Lambda}\otimes\boldsymbol{\Lambda}}{\boldsymbol{\Lambda}:\boldsymbol{\sigma}} : \boldsymbol{\sigma}, \tag{19c}$$

and

$$D = \frac{\xi}{2g_f}\frac{\partial \mathcal{K}}{\partial \kappa^{pd}}\boldsymbol{\sigma} : \frac{\boldsymbol{\Lambda}\otimes\boldsymbol{\Lambda}}{\boldsymbol{\Lambda}:\boldsymbol{\sigma}} : \boldsymbol{\sigma}. \tag{19d}$$

The rate constitutive law is given by:

$$\dot{\boldsymbol{\sigma}} = \mathbf{D}^t : \dot{\boldsymbol{\varepsilon}} \tag{20}$$

where the material tangent constitutive tensor is:

$$\mathbf{D}^t = \mathbf{D} - \frac{\left[(1-\xi)\mathbf{D} : \boldsymbol{\Lambda} + \xi\mathbf{D} : \frac{\boldsymbol{\Lambda}\otimes\boldsymbol{\Lambda}}{\boldsymbol{\Lambda}:\boldsymbol{\sigma}} : \boldsymbol{\sigma}\right] \otimes [\boldsymbol{\Lambda} : \mathbf{D}]}{A + B + C + D}. \tag{21}$$

2.1. Return mapping algorithm

The proposed methodology is solved in an incremental-iterative way. With this approach, at each integration point of the FE mesh, the objective is to compute the updated state variables $\boldsymbol{\varepsilon}^p_{t+\Delta t}$, $\kappa^{pd}_{t+\Delta t}$, $\mathcal{K}_{t+\Delta t}$ and $\mathbf{D}_{t+\Delta t}$ (at time $t+\Delta t$) from the information of the previous step (time t) and the prescribed strain increment $\boldsymbol{\Delta\varepsilon}$.

Following Meschke et al. [13], the updated stress can be obtained as

$$\boldsymbol{\sigma}_{t+\Delta t} = \mathbf{D}_n\,\boldsymbol{\varepsilon}^e_{t+\Delta t} = \boldsymbol{\sigma}^{trial}_{t+\Delta t} - \mathbf{D}_n\boldsymbol{\Delta\varepsilon}^p + \boldsymbol{\Delta}\mathbf{D}\boldsymbol{\varepsilon}^e_{t+\Delta t} \tag{22}$$

being $\boldsymbol{\sigma}^{trial}_{t+\Delta t} = \mathbf{D}_n(\boldsymbol{\varepsilon}_{t+\Delta t} - \boldsymbol{\varepsilon}^p_t)$ and $\mathbf{D}_n$ the secant constitutive tensor of the previous iteration. If the yield surface $\mathcal{F}(\boldsymbol{\sigma}^{trial}_{t+\Delta t}, \mathcal{K}_t) \leq 0$ is satisfied, the trial stress is physically admissible and the constitutive law integration is fulfilled. Conversely, if $\mathcal{F}(\boldsymbol{\sigma}^{trial}_{t+\Delta t}, \mathcal{K}_t) > 0$, an increment of damage and/or plastic strain has to be estimated via a backward Euler integration scheme.

After some mathematics, the updated stresses at $t+\Delta t$ is obtained, in a form analogously to plasticity, as

$$\boldsymbol{\sigma}_{t+\Delta t} = \boldsymbol{\sigma}^{trial}_{t+\Delta t} - \mathbf{D}_n\dot{\lambda}\boldsymbol{\Lambda}. \tag{23}$$

The updated internal variables $\mathbf{C}_{t+\Delta t}$, $\kappa^{pd}_{t+\Delta t}$, $\boldsymbol{\varepsilon}^p_{t+\Delta t}$ are obtained via Eqs. (12), (15) and (11), respectively. In order to update the material threshold $\mathcal{K}_{t+\Delta t}$, the selected hardening curve (Section 4) must be solved with the latest value of $\kappa^{pd}_{t+\Delta t}$.

3. Crack opening and re-closure: stiffness recovery effect

This section details the generalizations that must be made to the proposed model in order to model the effect of crack re-closure. Phenomenologically speaking, the stress recovery effect occurs when, after the material cracks due to a tensile load, it can close these cracks when the load is reversed, i.e. when the load becomes compressive. This effect is not generally captured in standard damage models [1].

To achieve this, the compliance tensor and its increments described in Eq. (12) have to be divided into a tensile $\dot{\mathbf{C}}_t$ and compressive $\dot{\mathbf{C}}_c$ parts:

$$\dot{\mathbf{C}}_t = r\,\xi\,\dot{\lambda}\,\frac{\boldsymbol{\Lambda}\otimes\boldsymbol{\Lambda}}{\boldsymbol{\Lambda}:\boldsymbol{\sigma}} \tag{24}$$

and

$$\dot{\mathbf{C}}_c = (1-r)\,\xi\,\dot{\lambda}\,\frac{\boldsymbol{\Lambda}\otimes\boldsymbol{\Lambda}}{\boldsymbol{\Lambda}:\boldsymbol{\sigma}}, \tag{25}$$

where the r parameter ranges from 0 (pure compression) to 1 (pure tension) as defined in Eq. (16). By using this split of the compliance increment, one can accumulate the stiffness loss in tension and compression separately depending on the characteristics of the stress tensor. Next, the total compliance tensor $\mathbf{C}$ can be obtained according to

$$\mathbf{C} = r\,\mathbf{C}_t + (1-r)\,\mathbf{C}_c\,, \tag{26}$$

and finally retrieving the updated constitutive matrix by $\mathbf{D} = \mathbf{C}^{-1}$ taking into account a ponderated measure of the tensile and compressive damages.

If different hardening laws have to be used in tensile and compressive states, a split of the energy dissipation and uniaxial stress threshold should be used. In this regard, the calculation of the normalized plastic-damage energy dissipation increment in tension ($\dot{\kappa}_t^{pd}$) and in compression ($\dot{\kappa}_c^{pd}$) is performed as

$$\dot{\kappa}_t^{pd} = \frac{1}{g_f}\left(\boldsymbol{\sigma} : \dot{\boldsymbol{\varepsilon}}^p + \frac{1}{2}\boldsymbol{\sigma} : \dot{\mathbf{C}}_t : \boldsymbol{\sigma}\right) \tag{27}$$

and

$$\dot{\kappa}_c^{pd} = \frac{1}{g_f}\left(\boldsymbol{\sigma} : \dot{\boldsymbol{\varepsilon}}^p + \frac{1}{2}\boldsymbol{\sigma} : \dot{\mathbf{C}}_c : \boldsymbol{\sigma}\right). \tag{28}$$

Following this approach, the energy dissipation of the plastic process is always accounted both in tension and in compression. Finally, in order to estimate the uniaxial threshold $\mathcal{K}$ that defines the elastic domain, we proceed analogously to Eq. (26):

$$\mathcal{K} = r \cdot \mathcal{K}_t(\kappa_t^{pd}) + (1-r) \cdot \mathcal{K}_c(\kappa_c^{pd}), \tag{29}$$

being $\mathcal{K}_t$ and $\mathcal{K}_c$ the tensile and compressive uniaxial thresholds computed as a function of its corresponding energy dissipation as shown in next section.

By using the split in terms of the energy dissipation and uniaxial stress threshold, different hardening laws and fracture energies can be used for tensile and compressive processes. In mixed mode loading problems, a consistent ponderation of the tensile and compressive components is considered.

3.1. Minimal numerical example considering crack opening and re-closure

A small numerical example is presented to demonstrate the capabilities of the proposed model in the capturing stress-recovery effects. The geometry consists in 1 mm height 3D cube. The element is fixed in one end and an imposed displacement is applied on the other side. The boundary conditions allow the Poisson deformations. The material properties considered are defined in Table 1. A Von-Mises yield surface was used together with an exponential softening law.

Initially, the cube is stretched until a certain level of degradation is achieved. Then, the imposed displacement is reversed. One can analyse in Fig. 2(a) how, when the imposed load changes from tension to compression, the stiffness of the material is recovered. This behaviour is maintained up to the yield stress in compression, when degradation continues. Fig. 2(b) depicts the energy dissipation during the load process, which includes the dissipation due to damage and plasticity.

It is important to mention that, since in this case the loading is uniaxial, the stresses are totally in tension or in compression, which means that the r parameter is either 0 (pure tension) or 1 (pure compression). This implies that the stress-recovery due to the load reversal is fully performed, regaining initial stiffness. In a mixed mode loading (see Section 5.5), since a ponderated part of tensile and compressive degradation is performed simultaneously, a lower stress recovery can be expected after a load reversal.

4. Non-linear energy dissipation-based hardening laws

In this section, the hardening/softening relations (hardening curves from now on) between stresses and strains are given. The hardening curves used in this paper are based on the work of Oller et al. [9,27] in which several mathematical expressions are provided for linear and exponential softening and parabolic hardening in the framework of plasticity. These curves (depicted in Fig. 3) were formulated for plasticity processes and they were based on the so-called *normalized plastic energy dissipation* κ^p.

Table 1
Tensile test material properties.

Variable	Value	Units
Young Modulus E	30	GPa
Poisson ratio ν	0.3	
Tensile strength f_t	5	MPa
Fracture energy tension G_f	10	J/m^2
Plastic-Damage distribution ξ	0.5	

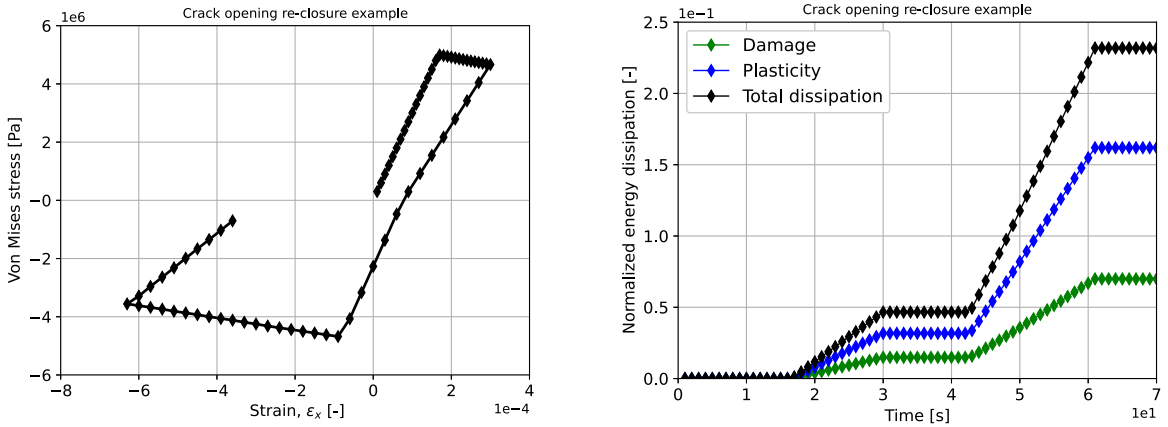

(a) Strain-Von Mises stress evolution

(b) Energy dissipation evolution

Fig. 2. Stress–Strain and energy dissipation evolution of the crack opening and re-closure example.

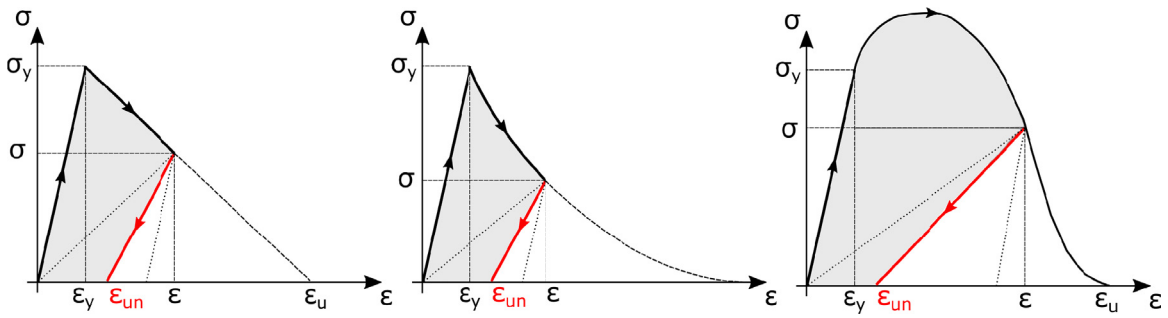

(a) Linear softening

(b) Exponential softening

(c) Parabolic hardening

Fig. 3. Different hardening/softening stress- strain behaviours. (For interpretation of the references to colour in this figure legend, the reader is referred to the web version of this article.)

In this work, the aforementioned curves have been used and adapted in order to reproduce the same behaviour in the new plastic-damage model. In order to do so, one has to employ the already exposed plastic-damage normalized energy dissipation κ^{pd} in Eq. (14) instead to the former κ^{p}. This implies the mathematical definition of the hardening laws according to the new κ^{pd}.

The three hardening curves used in this work are described. As it will be studied in the following Section, it is possible to obtain an analytical expression of the stress threshold according to the combined plastic-damage energy dissipation κ^{pd} for the linear softening case. However, for the exponential and parabolic hardening, it is not possible to obtain an explicit relationship between the threshold and the κ^{pd}. In these cases, an implicit calculation of the threshold is performed via a standard Newton–Raphson procedure and the value of its partial derivative $\frac{\partial \mathcal{K}}{\partial \kappa^{pd}}$ is also numerically estimated.

4.1. Linear softening

Simplifying the problem, one can suppose that the uniaxial behaviour of the material in tension, after the elastic loading branch, initiates a linear softening process like it is shown in Fig. 3(a), i.e.

$$\mathcal{K} = \sigma_y \left(\frac{\varepsilon_u - \varepsilon}{\varepsilon_u - \varepsilon_y} \right) \tag{30}$$

being σ_y the initial uniaxial stress threshold and ε_y its corresponding strain, ε_u the total strain value which corresponds to the total failure of the material and $\mathcal{K}$ the current uniaxial stress threshold.

As can be seen in Fig. 3, the unloading branch behaviour will depend on the plastic-damage proportion assigned to the material, being fully plastic when $\xi = 0$ and damage when $\xi = 1$. Indeed, in the unloading branch, the evolution of the stress will adopt the form:

$$\sigma = A \cdot \varepsilon + B, \tag{31}$$

being A and B scalar values. If one forces the curve defined in Eq. (31) to connect the current loading state (ε, σ) with its intersection with the abscesses axis $(\varepsilon_{un}, \sigma = 0)$ (see red branch in Fig. 3) one can obtain that:

$$\sigma(\varepsilon_{unloading}) = \left(1 + \frac{\varepsilon_{unloading} - \varepsilon}{\xi\varepsilon + (1-\xi)\varepsilon_y \frac{\varepsilon_u - \varepsilon}{\varepsilon_u - \varepsilon_y}} \right) \sigma_y \frac{\varepsilon_u - \varepsilon}{\varepsilon_u - \varepsilon_y} \tag{32}$$

where $\varepsilon_{unloading}$ corresponds to the independent strain variable in the unloading branch (red path in Fig. 3(a)).

Next, one can calculate the normalized energy dissipation consumed by the plastic-damage process (grey area in Fig. 3(a)) up to the current (ε, σ) state as:

$$\kappa^{pd} = \frac{1}{g_f} \left[\frac{1}{2}\sigma_y\varepsilon_y + \int_{\varepsilon_y}^{\varepsilon} \mathcal{K} d\varepsilon - \int_{\varepsilon_{un}}^{\varepsilon} \sigma(\varepsilon_{unloading}) d\varepsilon \right] \tag{33}$$

where the volumetric fracture energy is computed as $1/g_f = \left(\frac{r}{g_t} + \frac{1-r}{g_c} \right)$ ponderated over the tension and compression fracture energies depending on the r parameter which ranges from 0 (pure compression) to 1 (pure tension).

Inserting Eqs. (30) and (32) into Eq. (33) and solving the integrals one can obtain:

$$\kappa^{pd} = \frac{1}{g_f} \left[\frac{1}{2}\sigma_y\varepsilon_y + \frac{1}{2}(\varepsilon - \varepsilon_y)(\mathcal{K} + \sigma_y) - \frac{1}{2}\mathcal{K}(\varepsilon - \varepsilon_{un}) \right], \tag{34}$$

Combining Eqs. (30), (32) and (34), and after some mathematical manipulation one can state a closed analytical form that relates the updated stress threshold $\mathcal{K}$ with the normalized plastic-damage energy dissipation κ^{pd} as

$$\mathcal{K} = \sigma_y \frac{\sqrt{(2-\xi)^2 - 4\kappa^{pd}(1-\xi)} - \xi}{2(1-\xi)} \tag{35}$$

and its partial derivative to be used in Eq. (18) can be retrieved as

$$\frac{\partial \mathcal{K}}{\partial \kappa^{pd}} = \frac{-\sigma_y}{\sqrt{(2-\xi)^2 - 4\kappa^{pd}(1-\xi)}} \tag{36}$$

4.2. Exponential softening

In pure tension, it is also possible to use softening functions that better approximate the behaviour of concrete. There are a large number of such functions that have been formulated from experimental studies. A simple exponential function (Fig. 3(b)) has been considered here [9,27] that approximates quite well compared other

more complex expressions that have been proposed for the simulation of the behaviour of concrete in tension with softening. That is:

$$\mathcal{K} = \sigma_y \exp\left(\frac{\sigma_y(\varepsilon - \varepsilon_y)}{\frac{1}{2}\sigma_y\varepsilon_y - g_f}\right). \tag{37}$$

Analogously to the linear softening case, one can obtain the expression of the unloading branch:

$$\sigma(\varepsilon_{unloading}) = \sigma_y \left(1 + \frac{\varepsilon_{unloading} - \varepsilon}{\varepsilon\xi + (1-\xi)\varepsilon_y \exp\left(\frac{\sigma_y(\varepsilon-\varepsilon_y)}{\frac{1}{2}\sigma_y\varepsilon_y - g_f}\right)}\right) \exp\left(\frac{\sigma_y(\varepsilon - \varepsilon_y)}{\frac{1}{2}\sigma_y\varepsilon_y - g_f}\right) \tag{38}$$

By using the same equation for calculating the normalized plastic-damage dissipation defined in Eq. (33) and inserting Eqs. (37) and (38), one can obtain an implicit relationship between the stress threshold $\mathcal{K}$ and the normalized plastic-damage energy dissipation κ^{pd} for the exponential softening case as

$$\sigma_y\,(1-\kappa^{pd}) = \tag{39}$$

$$\mathcal{K}\left\{1 + \frac{\sigma_y\,\varepsilon_y}{2g_f}\left[(1-\xi)\left(\frac{\mathcal{K}}{\sigma_y} - \frac{1}{2}\ln\left(\frac{\mathcal{K}}{\sigma_y}\right) - 1\right) + \frac{1}{2}\ln\left(\frac{\mathcal{K}}{\sigma_y}\right)\right] - \frac{\xi}{2}\ln\left(\frac{\mathcal{K}}{\sigma_y}\right)\right\} \tag{40}$$

As can be seen in Eq. (40), there is not a straight forward way of obtaining an explicit equation of the stress threshold for a certain energy dissipation κ^{pd}. This issue is circumvented by implementing a simple local Newton–Raphson strategy that, for a given value of κ^{pd}, iteratively approximates its corresponding updated stress threshold $\mathcal{K}$. Indeed, the implicit function $\mathcal{F}(\mathcal{K}, \kappa^{pd})$ to be minimized is

$$\mathcal{F}(\mathcal{K}, \kappa^{pd}) = \sigma_y\,(1-\kappa^{pd}) - \mathcal{K}\left\{1 + \frac{\sigma_y\,\varepsilon_y}{2g_f}\left[(1-\xi)\left(\frac{\mathcal{K}}{\sigma_y} - \frac{1}{2}\ln\left(\frac{\mathcal{K}}{\sigma_y}\right) - 1\right)\frac{1}{2}\ln\left(\frac{\mathcal{K}}{\sigma_y}\right)\right] - \frac{\xi}{2}.\ln\left(\frac{\mathcal{K}}{\sigma_y}\right)\right\} \tag{41}$$

of which its partial derivative with respect to $\mathcal{K}$ can be easily found in order to update iteratively the values of $\mathcal{K}$ for a given κ^{pd}.

Finally, since no explicit expression of $\mathcal{K}$ is known, the computation of its partial derivative to be used in Eq. (18) can be estimated accurately by using finite differences. Indeed, if a forward Euler scheme is used, a good approximation of the derivative is obtained by:

$$\frac{\partial \mathcal{K}}{\partial \kappa^{pd}} \approx \frac{\mathcal{K}(\kappa^{pd} + \delta\kappa^{pd}) - \mathcal{K}(\kappa^{pd})}{\delta\kappa^{pd}}, \tag{42}$$

in which $\mathcal{K}(\kappa^{pd} + \delta\kappa^{pd})$ and $\mathcal{K}(\kappa^{pd})$ are computed implicitly by minimizing Eq. (41). A consistent value for the perturbation $\delta\kappa^{pd}$ has been found to be 10^{-7}.

4.3. Parabolic hardening

For a more general case in compression of frictional materials, a different curve is proposed. This is a function of the normalized plastic-damage energy dissipation κ^{pd} composed by an initial hardening reaching a maximum stress $\mathcal{K}^{peak}$ followed by a softening branch (Fig. 3(c)).

An analytical expression of the curve in the $\mathcal{K} - \varepsilon$ space that agrees with experimental data, both in tension and in compression, is given by the following expression:

$$\mathcal{K} = \sigma_y\left[\chi(1-a)\exp(-b(\varepsilon - \varepsilon_y)) - a\exp(-2b(\varepsilon - \varepsilon_y))\right] \tag{43}$$

where

$$a = \frac{\chi - 1}{\chi + 1} \quad ; \quad b = \frac{\sigma_y}{2\left(g_f - \frac{1}{2}\varepsilon_y\sigma_y\right)}\frac{3\chi + 1}{\chi + 1} \tag{44}$$

If the hardening curve is tangent to the initial elastic branch, the χ parameter has to be:

$$\chi = \frac{\sigma_y \varepsilon_y + g_f + \sqrt{\frac{5}{4}\sigma_y \varepsilon_y + 2g_f}}{\frac{1}{2}\sigma_y \varepsilon_y - g_f} \tag{45}$$

and its corresponding maximum stress is computed as:

$$\sigma_{max} = \frac{\chi^2 \sigma_y}{\chi^2 - 1}. \tag{46}$$

However, if the maximum stress is set as a material property, the χ parameter will be computed as

$$\chi = -\sqrt{\frac{\sigma_{max}}{\sigma_{max} - \sigma_y}}. \tag{47}$$

After some mathematical manipulation, and ensuring that the loading process dissipates a maximum amount of volumetric energy g_f, one can state that the implicit function $\mathcal{F}(\mathcal{K}, \kappa^{pd})$ that relates the uniaxial stress threshold and the energy dissipation to be minimized is ($n = 1$ in hardening and $n = 2$ in softening)

$$\mathcal{F}(\mathcal{K}, \kappa^{pd}) = \frac{\sigma_y \varepsilon_y \left[1 - \left(\frac{\mathcal{K}}{\sigma_y}\right)^2 \left(1 + \left(\frac{\mathcal{K}}{\sigma_y}\right)\xi - \xi\right)\right]}{2g_f}$$
$$+ \frac{\frac{1}{2}\sigma_y \varepsilon_y - g_f}{g_f(3\chi + 1)(\chi - 1)} \left[\left(1 + (-1)^n \alpha\right)\left(2\chi + 1 - (-1)^n \alpha\right) - \frac{\mathcal{K}}{\sigma_y}(\chi^2 - 1)\xi \ln\left(\frac{\chi + (-1)^n \alpha}{\chi - 1}\right)\right] - \kappa^{pd} = 0 \tag{48}$$

being

$$\alpha = +\sqrt{\chi^2 \left(1 - \frac{\mathcal{K}}{\sigma_y}\right) + \frac{\mathcal{K}}{\sigma_y}}. \tag{49}$$

Analogously to the previous softening case, solving numerically the proposed implicit equation for each level of energy dissipation will provide its corresponding updated stress threshold. Additionally, the partial derivative of the stress threshold with respect to the normalized energy dissipation can be also estimated by Eq. (42).

It is important to note that, conversely to the exponential softening case, the implicit solving of Eq. (48) is not straight forward. In order to circumvent these numerical inconveniences, several strategies should be employed. Fig. 4 depicts the evolution of the implicit equation (Eq. (42)) as a function of the stress threshold to be solved numerically for a certain level of normalized plastic-damage energy dissipation κ^{pd}. As can be seen in the previous figure, the hardening branch has a local minimum around $\mathcal{K} \approx 5.5e8$ Pa. This implies that one has to check whether the initial guess of the Newton–Raphson coincides with the mentioned $\mathcal{K}$. Indeed, this happens for example when $\kappa^{pd} = 0$ and use the initial stress threshold as an initial guess.

Another problematic scenario arises when the hardening curve is reaching the peak stress. At this point, the partial derivative of the implicit function $\mathcal{F}(\mathcal{K}, \kappa^{pd})$ becomes infinite around the root surroundings. This numerical issue can be avoided by setting the maximum allowable value of the threshold close to the peak with a certain tolerance. Whenever this happens, the hardening curve moves automatically to the softening branch, which exhibits total stability.

5. Numerical examples

A selection of numerical examples is given in this section in order to show the efficiency and accuracy of the proposed coupled plastic-damage model for cyclic loading. The geometries consist of three-dimensional models and the results obtained are compared against experimental results and other numerical approaches. The implementation of the proposed methodology has been done inside the open-source Kratos-Multiphysics FE code [28,29]

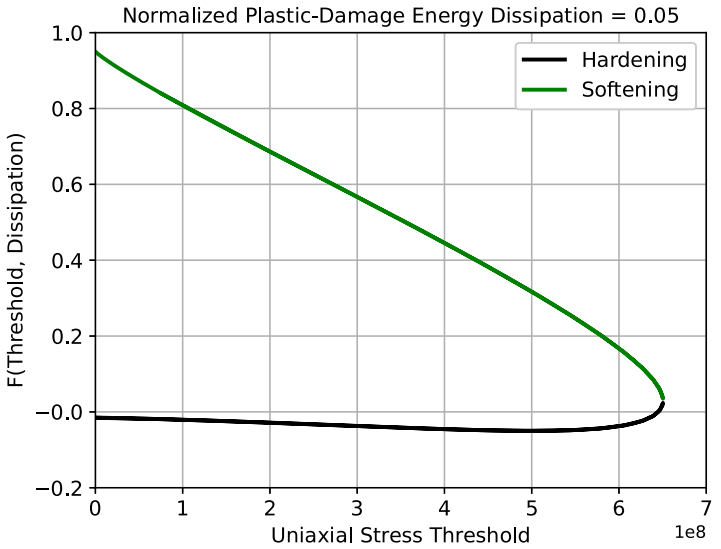

Fig. 4. Evolution of the implicit equation to be minimized $\mathcal{F}(\mathcal{K}, \kappa^{pd})$ for a given κ^{pd} showing the hardening and softening branches.

The first set of examples consists in cyclic uniaxial tensile and compressive tests, employing the softening and hardening laws presented in the previous section, respectively. The second example reproduces a three point bending test of a notched beam under a cyclic vertical loading. Finally, a uniaxial compression test of a cylindrical sample is conducted.

The numerical results are compared with experimental and the data obtained with other numerical techniques.

5.1. Tensile and compressive cyclic tests

In order to assess the accuracy of the proposed rate-independent plastic-damage model, a uniaxial cyclic tensile and compressive test is performed. The results obtained are compared against the experimental data provided by Karsan and Jirsa [30].

The geometry of these examples consists in a single hexahedron with dimensions 82.6 × 82.6 × 82.6 mm. This geometry is submitted to a cyclic tension or compression state. The material properties used in the tensile and compressive test are given in Tables 2 and 3, respectively. A Drucker–Prager yield surface has been chosen, suitable for concrete type materials submitted to tension and/or compression. In the tensile test an exponential softening type (Section 4.2) has been selected, whereas in the compressive test a parabolic hardening (Section 4.3) is employed. For the sake of completeness, the linear softening law has been also used in order to compare the different material behaviours.

Fig. 5 shows the results obtained with the proposed model are in good agreement with the experimental data available both for the tensile and compressive tests. As Lee and Fenves [22] mention, the experimental data provided by Karsan and Jirsa [30] in the tensile case shows a very steep post-peak slope (Fig. 5(a)) induced by the use of a wide strain gauge over the localized zone for measuring the results. This explains the slight difference between the numerical and experimental results. This example shows that the proposed hardening/softening laws based on the plastic-damage energy dissipation κ^{pd} can reproduce efficiently the tension and compression behaviour of concrete, with a minimal calibration of the input parameters χ and $\mathcal{K}_0$ in the compressive test.

The evolution of the new internal variable κ^{pd} for different strain states is depicted in Fig. 6. As shown in the previous figures, the reversion of the load induces a stabilization of the energy dissipation. In the case of the cyclic tensile test, the dissipated energy is almost the total available ($\kappa^{pd} \approx 1$). On the contrary, in the cyclic compressive test, only the 40% of the total energy has been consumed in the whole process.

Table 2
Tensile test material properties.

Variable	Value	Units
Young Modulus E	31	GPa
Poisson ratio ν	0.18	
Tensile strength f_t	3.48	MPa
Fracture energy tension G_f	40	J/m^2
Plastic-Damage distribution ξ	0.5	

Table 3
Compressive test material properties.

Variable	Value	Units
Young Modulus E	31.7	GPa
Poisson ratio ν	0.18	
Compressive yield strength f_c	15	MPa
Fracture energy compression G_c	5690	J/m^2
Peak stress position χ	0.08	
Peak stress $\mathcal{K}^{peak}$	27.6	MPa
Plastic-Damage distribution ξ	0.5	

Table 4
Three point bending test material properties.

Variable	Value	Units
Young Modulus E	43.6	GPa
Poisson ratio ν	0.2	
Tensile yield strength f_t	4.0	MPa
Compressive yield strength f_c	63.4	MPa
Fracture energy tension G_f	119.5	J/m^2
Fracture energy compression G_c	5975	J/m^2
Plastic-Damage distribution ξ	0.5	

5.2. Three point bending cyclic test

A notched concrete beam submitted to cyclic loading is studied in this section. This example has been performed experimentally by Perdikaris and Romeo [31] and numerically reproduced in Meschke et al. [13].

Figs. 7 and 8 depict the geometry of the notched concrete beam and the FE mesh used in this work, respectively. The 3D FE mesh consists in 9665 nodes and 7376 linear B-bar hexahedra elements. The thickness of the beam is 127 mm [31].

The sample is tested under displacement control, by increasing/decreasing the imposed vertical displacement according to the experiment. The material properties [13] used in the calculation are given in Table 4. The yield criterion used is the Drucker–Prager yield surface. Since mode I of fracture is expected as the notch tip, an exponential softening law is assumed as a dominant behaviour in this simulation.

Fig. 10 depicts the force-CMOD (Crack Mouth Opening Displacement) evolution of the structure for the proposed method, experimental results [31] and the data given in Meschke et al. [13]. As one can see in Fig. 10, the peak load and the post-peak behaviour of the sample is well captured according the experiment and in very good agreement with the results proposed by Meschke et al. [13].

Fig. 9 shows the plastic dissipation κ^{pd} field for different CMOD snapshots. The fracture correctly localizes in a single FE and evolves upwards vertically as expected, according to the experiments.

5.3. Concrete sample under compressive cyclic loading

This example consists in a numerical simulation of an experiment conducted by Osorio et al. [32] in which a compressive cyclic test is performed to a concrete specimen. Both in the experiments and in the performed numerical simulation, the longitudinal strain is studied.

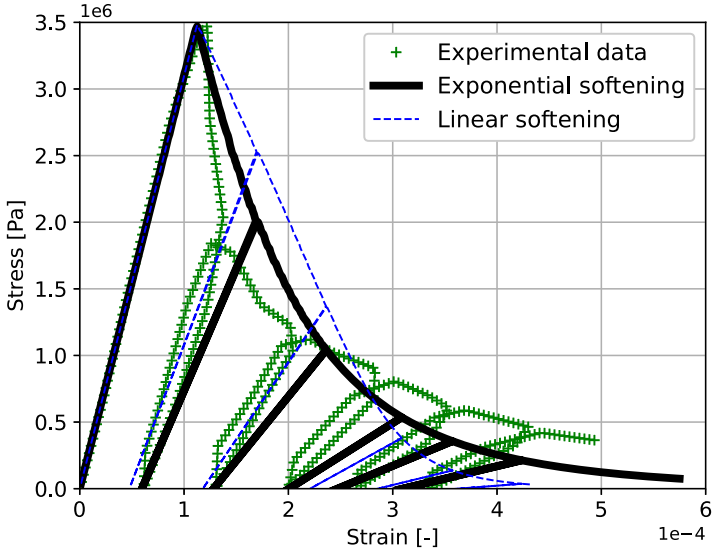

(a) Tensile cyclic test

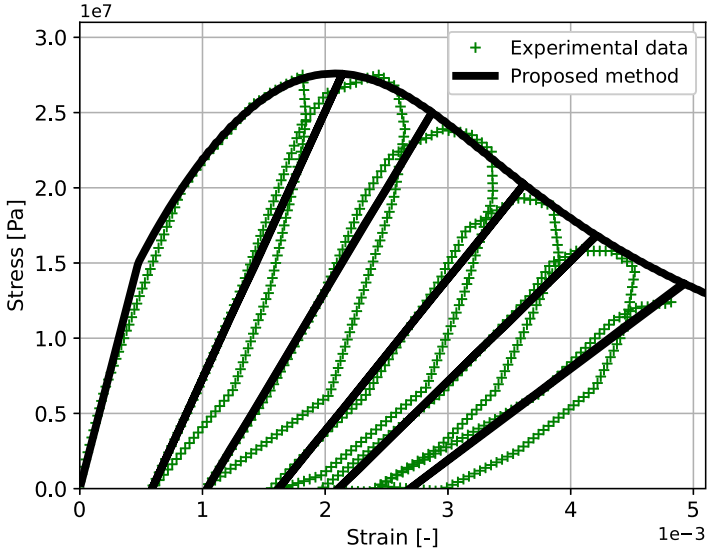

(b) Compressive cyclic test

Fig. 5. Uniaxial cyclic tests, stress–strain behaviour.

The sample corresponds to a 35 MPa concrete type employing Portland with limestone cement (CEM II/A-L) [32]. The original setup in Osorio et al. [32] can be seen in Fig. 11. The sample is cylindrical with 0.2 m height and 0.1 m of diameter. The FE mesh used is formed by 6806 nodes and 5760 B-bar hexahedra (Fig. 12). The simulated domain is one quarter of the whole sample, taking advantage of the symmetry of the problem. In the experiment, the top and bottom surfaces have been treated to avoid friction so in the numerical model only the vertical movement is restricted. The material properties are given in Table 5. The yield surface used is the Modified Mohr–Coulomb [15] yield criterion with a parabolic hardening law.

The results of the numerical simulation can be seen in Fig. 13. Clearly, the model is capable of reproducing the behaviour of the concrete sample both in the monotonic and cyclic loading. As expected, the rate-dependent

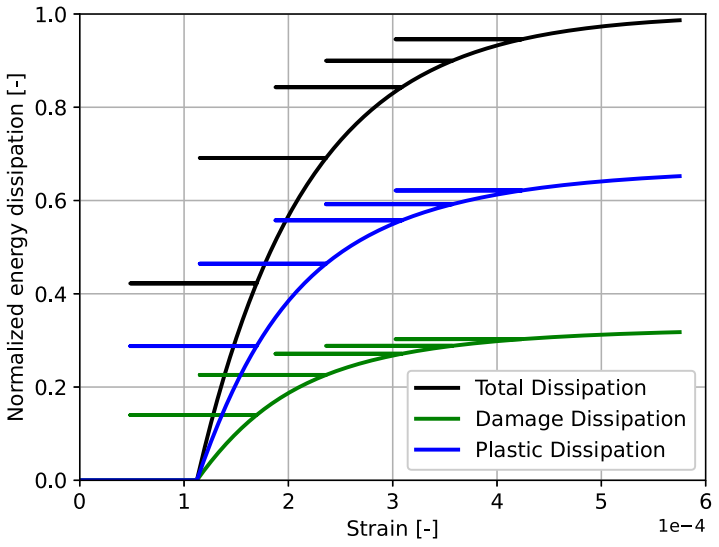

(a) Tensile cyclic test

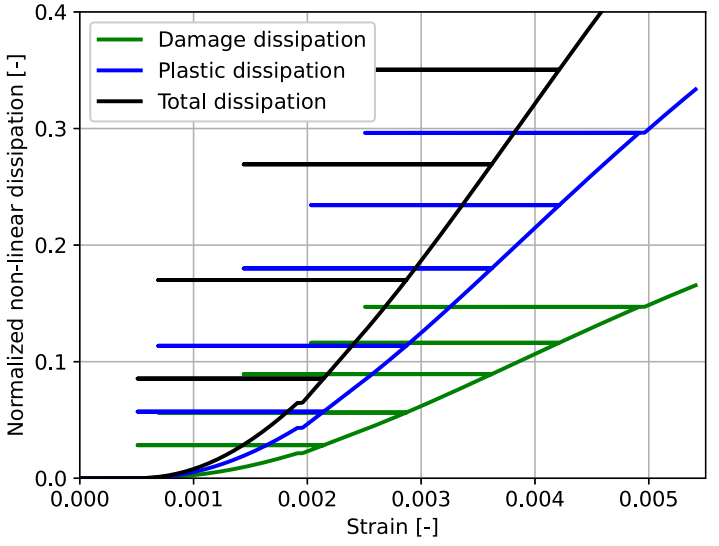

(b) Compressive cyclic test

Fig. 6. Uniaxial cyclic tests. Evolution of the new internal variable: the normalized plastic-damage dissipation κ^{pd}.

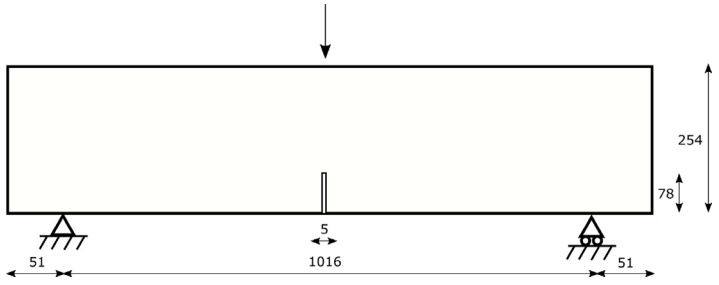

Fig. 7. Three point cyclic bending test geometry. Units in [mm].

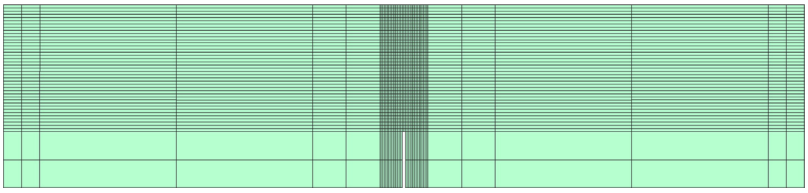

Fig. 8. Three point cyclic bending test FE mesh. 9665 nodes and 7376 linear hexahedra Bbar FE.

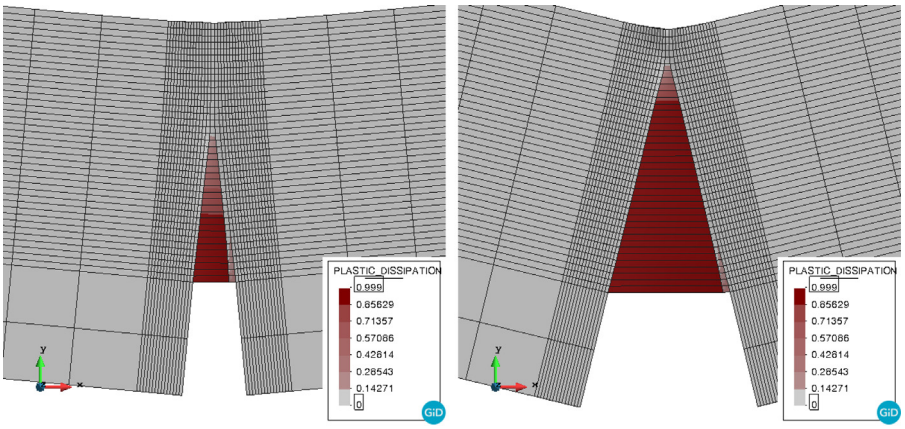

(a) CMOD $= 1.97 \cdot 10^{-4}$ m (b) CMOD $= 5.76 \cdot 10^{-4}$ m

Fig. 9. Three point cyclic bending test. Normalized plastic-damage energy dissipation field for two corresponding CMOD values, 200-fold magnification of the displacement field.

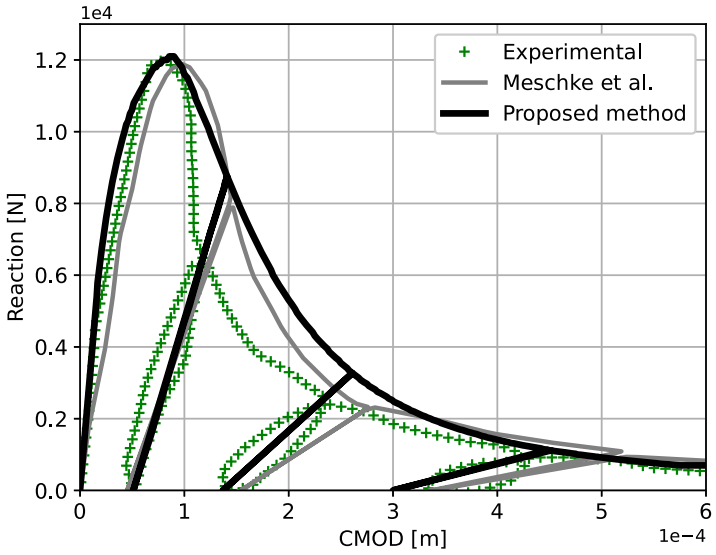

Fig. 10. Three point cyclic bending test. Force–displacement evolution.

Table 5
Compressive test of concrete sample. Material properties.

Variable	Value	Units
Young Modulus E	33 535	MPa
Poisson ratio ν	0.23	
Compressive yield strength f_c	20	MPa
Fracture energy compression G_c	9000	J/m^2
Peak stress position χ	0.2	
Peak stress $\mathcal{K}^{peak}$	37.4	MPa
Friction angle ϕ	32	Deg
Plastic-Damage distribution ξ	0.15	

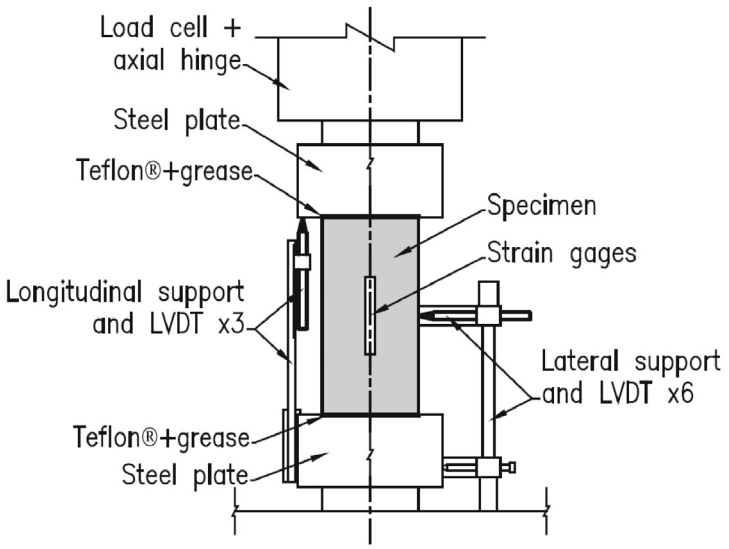

(a) Schematic representation of the assembly. Source: Osorio et al. [23].

(b) Test instrumentation used in the experiments. Source: Osorio et al. [23].

Fig. 11. Cyclic compression test. Experimental instrumentation.

variations exhibited in the experiment are not taken into account but the global stiffness and evolution are accurately obtained.

5.4. Mixed-mode Alvarez three point bending beam

In this case, a three point beam with an eccentric notch is studied. This example was conducted in Garcia-Alvarez et al. [33] and reproduced in Barbat et al. [34] and Cornejo et al. [35] as a mixed-mode fracture problem for assessing the mesh size-effect. The geometry used is depicted in Fig. 14.

In the studied case, D = 320 mm and the λ factor is 0.25. The thickness of the sample is 50 mm according to the literature. The notch eccentricity is selected to be $\mu D = 0.625D$. The material properties proposed by Garcia-Alvarez et al. [33] are given in Table 6. A B-bar small displacement element was employed and a Rankine yield surface and plastic potential were used in order to check the elastic domain and plastic flow calculation. The FE mesh used is depicted in Fig. 15. The notch has been discretized by 4 FE in order to properly capture the induced stress gradients.

As can be seen in Fig. 16, the fracture paths obtained by means of the proposed plastic-damage model is in accordance with the existing numerical solutions available in literature (Cornejo et al. and Barbat et al.). Moreover, the force-Crack Mouth Displacement (CMOD) evolution is also in agreement with the existing data as can be studied in Fig. 17. The correctness of the obtained results in this numerical example ensures the model's appropriateness for mixed mode fracture simulations.

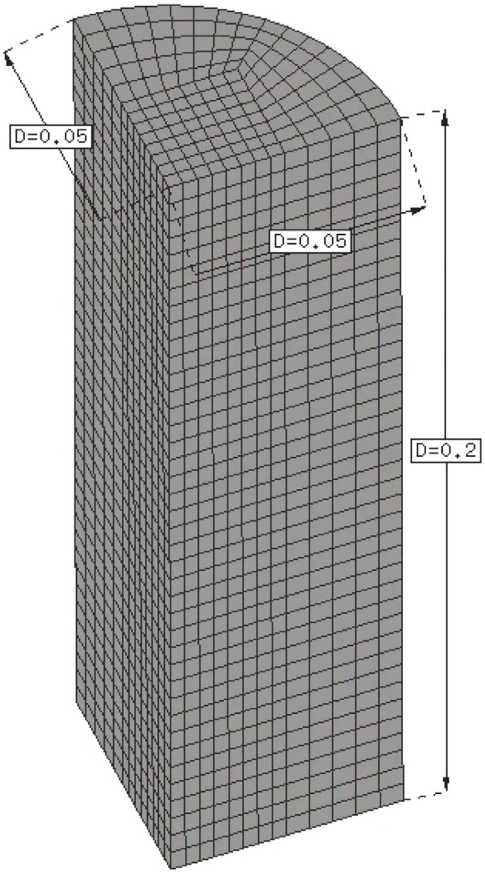

Fig. 12. Cyclic compression test. Geometry, dimensions and FE mesh of the sample (6806 nodes and 5760 B-bar hexahedra). Units in m.

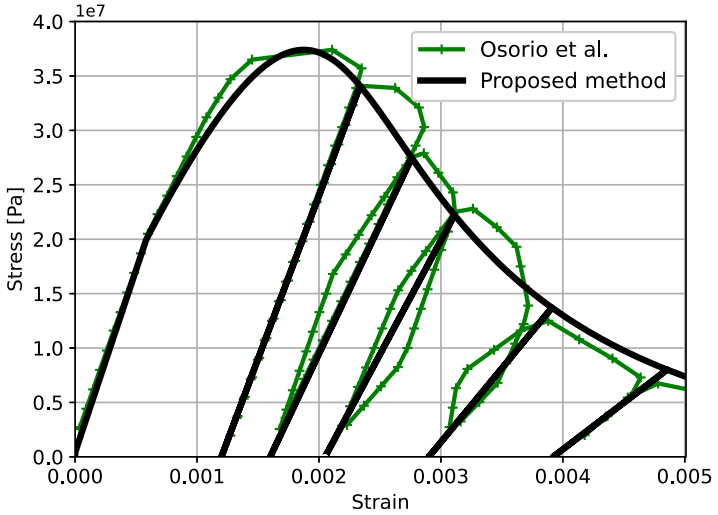

Fig. 13. Longitudinal stress–strain curve of the uniaxial compression test.

Table 6
Garcia-Alvarez mixed mode case. Material properties.

Variable	Value	Units
Young Modulus E	33.8	GPa
Poisson ratio ν	0.23	
Tensile yield strength f_c	3.5	MPa
Tensile Fracture energy f_c	80	J/m^2
Plastic-Damage distribution ξ	0.5	

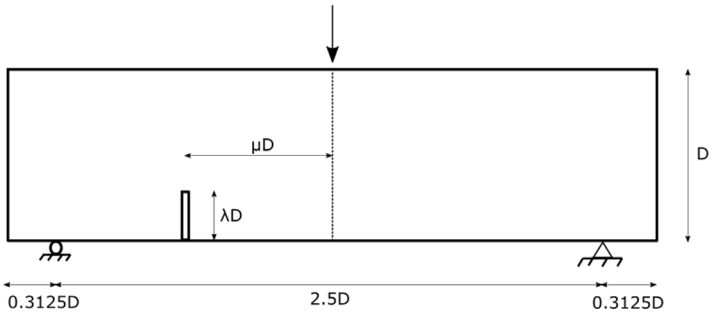

Fig. 14. Mixed Mode Garcia-Alvarez test geometry.

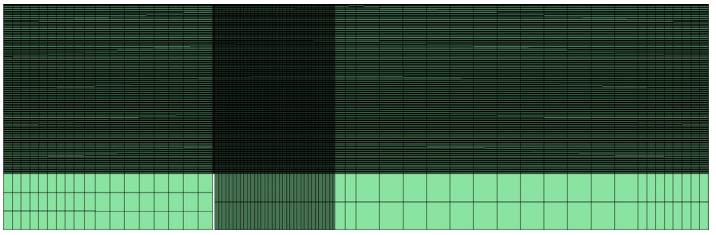

Fig. 15. Mixed Mode Garcia-Alvarez test FE mesh used composed by 118,196 nodes and 58,598 B-bar FE.

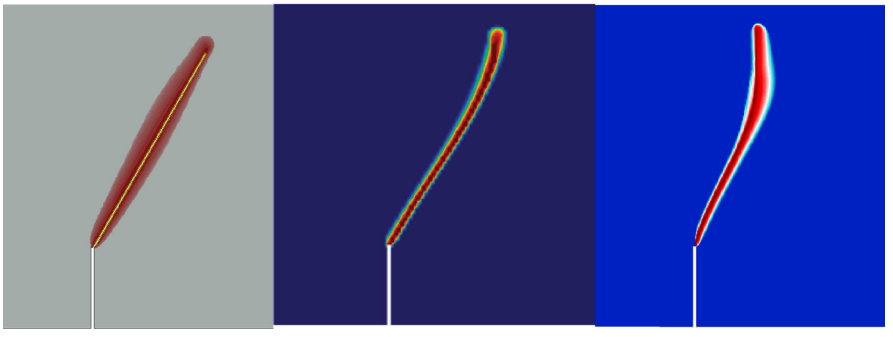

(a) Cornejo et al. (b) Barbat et al. (c) Proposed model

Fig. 16. Fracture paths obtained by Cornejo et al. [35], Barbat et al. [34] and with the proposed constitutive model.

5.5. Cyclic shear test

In this section, the numerical simulation of a cubic metal specimen subjected to shear cyclic loading is considered. This example consists in a 3D simulation of the geometry depicted in Fig. 18. An initial 0.1 mm length slit is introduced at the centre of the sample to initiate the fracture. For efficiency, only a thickness of 10^{-5} m is considered. A similar example can be found in Barbat et al. [1] where an orthotropic damage model was used and in [36–38]

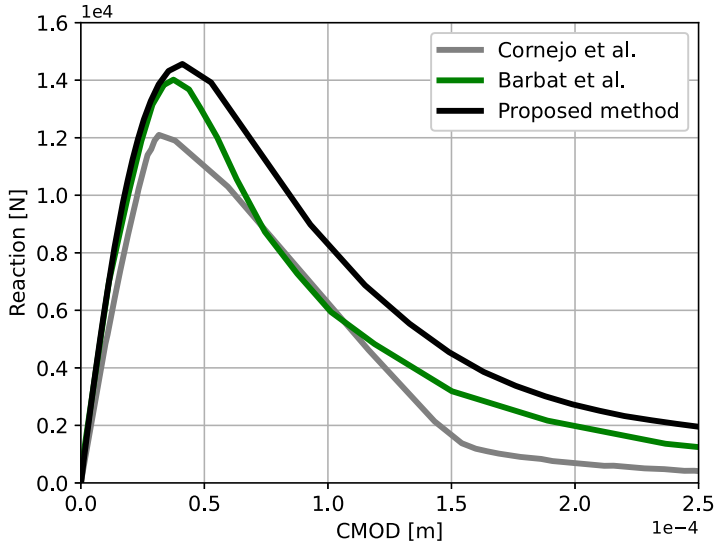

Fig. 17. Force-CMOD evolution for the Garcia-Alvarez mixed mode case. Comparison of the results obtained in Cornejo et al. [35], Barbat et al. [34] and with the proposed constitutive model.

Table 7
Cyclic shear test. Material properties.

Variable	Value	Units
Young Modulus E	30.0	GPa
Poisson ratio ν	0.3	
Tensile yield strength f_c	5.0	MPa
Tensile Fracture energy f_c	1.0	J/m^2
Plastic-Damage distribution ξ	0.5	
Friction angle ϕ	30.0	deg

where phase-field models are employed. The material properties used are defined in Table 7. In this example, a Drucker–Prager yield surface is considered together with an exponential softening flow rule.

The setup of the problem is depicted in Fig. 18. The base of the cube is totally fixed. The cyclic shear load is imposed by applying a horizontal displacement at the top of the sample. Finally, the vertical displacement of the lateral walls is also prevented.

This numerical example consists in a 3D simulation with plane strain conditions with a structured mesh of Bbar hexahedra elements of size $h = 10^{-5}$ m. In this case, a horizontal rightward displacement is imposed first (up to $t = 0.15$ s). Then, the imposed displacement is reversed, causing the material to degrade in the opposite direction ($t = 0.44$ s). Fig. 19 shows the displacement field obtained at the end of each loading process. One can clearly see the localization of the damage and plastic deformation and the effect of the irrecoverable strains when reversing the load. Figs. 20 and 21 depict the damage and plastic strain fields, respectively.

Finally, the force–displacement evolution of the shear test can be studied in Fig. 22. As expected, a simultaneous evolution of damage and plasticity is exhibited. As previously stated, since in this case the energy dissipation is developed in a mixed mode, the tensile and compressive stiffness degradation is ponderated according to r. This is the reason why the stress-recovery in this example is not that evident in comparison with the fully tensile/compressive example in Fig. 2.

6. Concluding remarks

The numerical results obtained in the examples analysed show that the constitutive model proposed in this paper is capable of simulating in an efficient and accurate way the behaviour of frictional and metallic materials under monotonic and cyclic loading conditions. The fact of using the dissipated energy as an internal variable of the

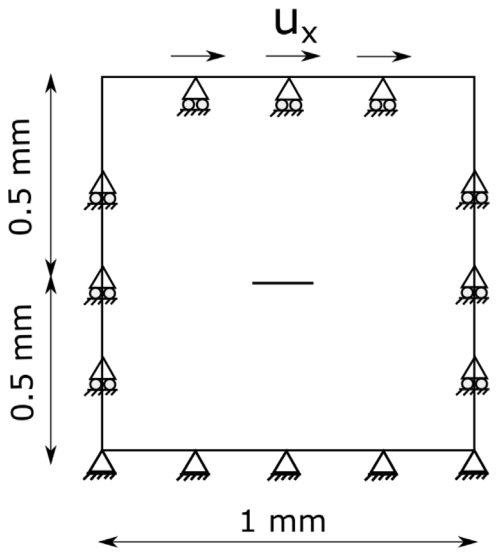

Fig. 18. Cyclic shear test geometry.

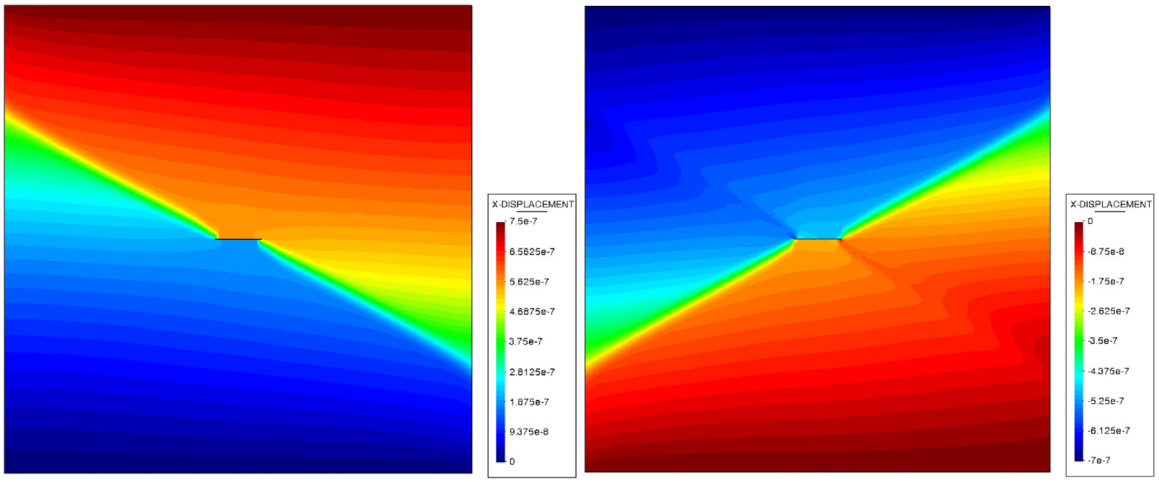

(a) t=0.15 s (b) t=0.44 s

Fig. 19. Cyclic shear test. Displacement field at different time steps. Units in m.

model instead of the accumulated plastic deformation, for example, ensures a correct mathematical and energetic consistency that is difficult to achieve with previous methods. Likewise, in case of possessing information regarding fracture energies in tension, compression and shear, it would be straightforward to include them in the model and accumulate their dissipation in an incremental way. Additionally, the energy methodology proposed for the hardening laws can automatically and naturally accommodate tensile and compressive processes without any change, except for the correct definition of the corresponding fracture energies. To achieve the above, it has been necessary to derive the corresponding mathematical expressions that give the model its mathematical consistency as well as its linearization and implementation. The derivation of the hardening equations as well as their implicit resolution and their partial derivative have been necessary to obtain the numerical results presented in the article.

The plastic-damage model has been generalized to be able to reproduce effectively crack opening and re-closure effects. This has been done by splitting the compliance matrices into a tensile and compressive parts. If different evolution laws have to be used in tension and in compression, a proper calculation of the energy dissipated in each

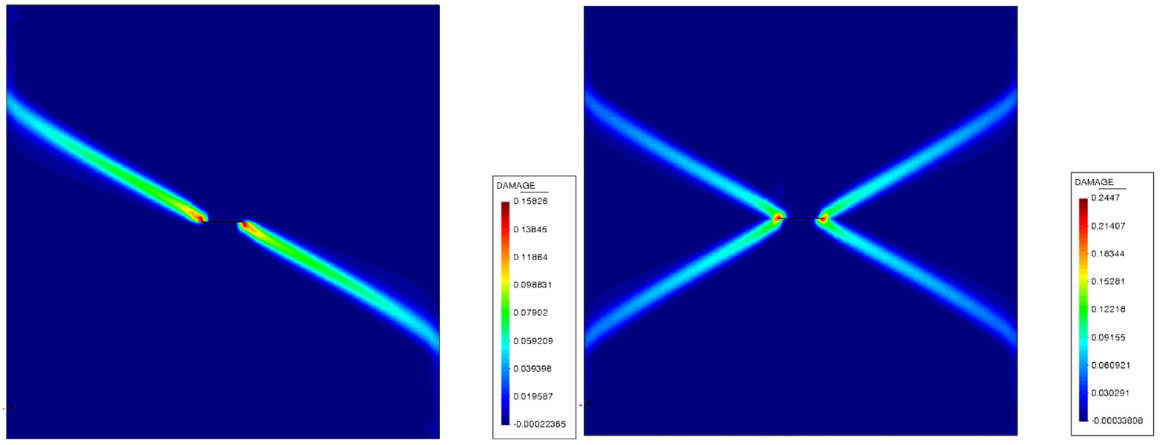

(a) t=0.15 s (b) t=0.44 s

Fig. 20. Cyclic shear test. Damage contours at different time steps.

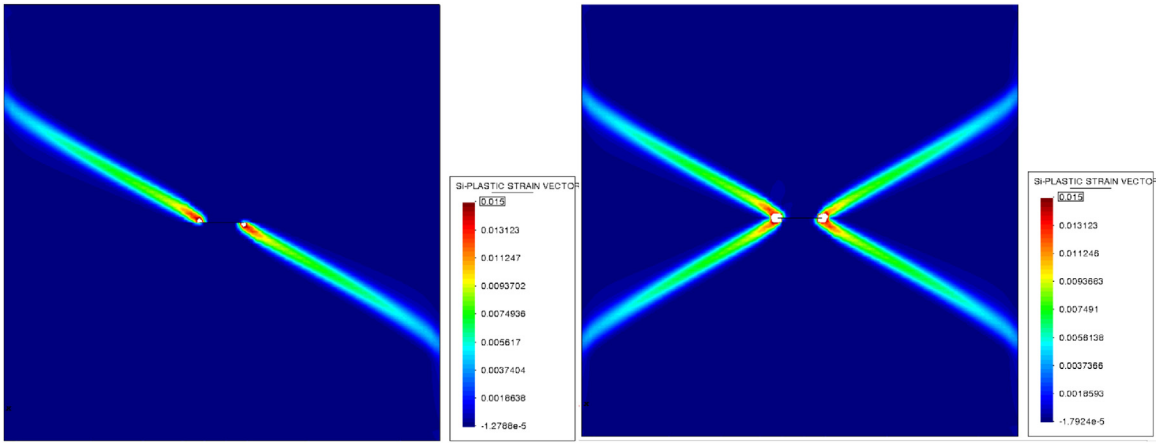

(a) t=0.15 s (b) t=0.44 s

Fig. 21. Cyclic shear test. Plastic strain contours at different time steps.

process has to be calculated. In this way, the stiffness degradation depends on the sign of the load in an energy consistent manner.

However, some improvements and generalizations can be added to the model in order to widen the range of engineering problems that could be potentially applied.

One enhancement of the model can be the inclusion of a combined isotropic and kinematic hardening. This would allow to better simulate the Bauschinger effect in case of total reversion of the load, i.e. changing the load from tension to compression or vice-versa. This implementation is easy to perform and no major modifications of the presented algorithm need to be done. The mentioned kinematic hardening affects the calculation of the plastic strain and the evolution of the material threshold.

One final addition to the model that can be useful consists in implementing an evolution of the dilatancy angle based on the degradation or plastification occurred. In this way, no extra calibration will be needed in problems sensitive to confinement or shear softening.

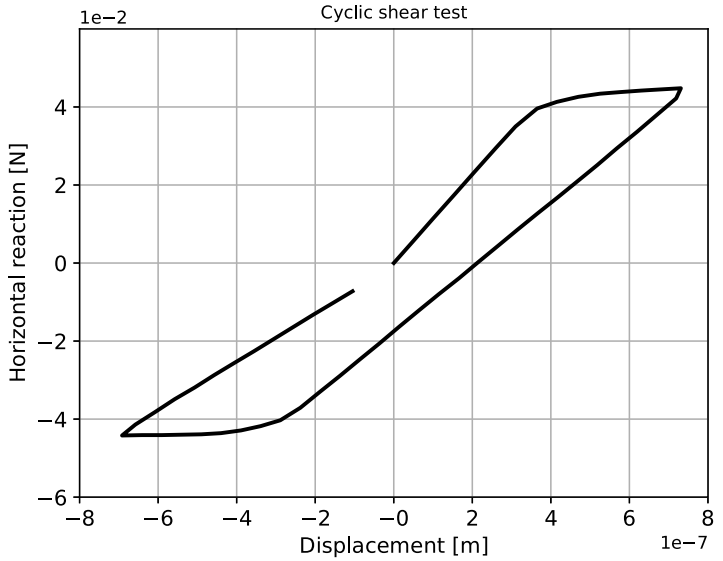

Fig. 22. Force–displacement evolution obtained in the cyclic shear test.

Declaration of competing interest

The authors declare that they have no known competing financial interests or personal relationships that could have appeared to influence the work reported in this paper.

Data availability

No data was used for the research described in the article.

Acknowledgements

This work has been done within the framework of the Fatigue4Light (H2020-LC-GV-06-2020) project: "Fatigue modelling and fast testing methodologies to optimize part design and to boost lightweight materials deployment in chassis parts". This project has received funding from the European Union's Horizon 2020 research and innovation programme under grant agreement No 101006844. The work has been also supported by the Spanish Government program FPU17/04196. The authors gratefully acknowledge all the received support. Finally, acknowledge the support received by the Severo Ochoa Centre of Excellence (2019–2023) under the grant CEX2018-000797-S funded by MCIN/AEI/10.13039/501100011033.

Appendix A. Derivation of the plastic consistency expression

In order to obtain the expression of a consistent plastic multiplier for the proposed internal variable κ^{pd}, one states initially the consistency condition:

$$\dot{\mathcal{F}} = \frac{\partial \mathcal{F}}{\partial \boldsymbol{\sigma}} : \dot{\boldsymbol{\sigma}} + \underbrace{\frac{\partial \mathcal{F}}{\partial \mathcal{K}}}_{-1} \dot{\mathcal{K}} = 0. \tag{A.1}$$

which implies that (Notation $\frac{\partial \mathcal{F}}{\partial \boldsymbol{\sigma}} := \boldsymbol{\Lambda}$)

$$\boldsymbol{\Lambda} : \dot{\boldsymbol{\sigma}} - \dot{\mathcal{K}} = 0. \tag{A.2}$$

Since $\mathcal{K} = \mathcal{K}(\kappa^{pd})$, one can rewrite

$$\boldsymbol{\Lambda} : \dot{\boldsymbol{\sigma}} - \frac{\partial \mathcal{K}}{\partial \kappa^{pd}} \dot{\kappa}^{pd} = 0, \tag{A.3}$$

and using Eq. (15)

$$\boldsymbol{\Lambda} : \dot{\boldsymbol{\sigma}} - \frac{\partial \mathcal{K}}{\partial \kappa^{pd}} \left(\boldsymbol{\sigma} : \dot{\boldsymbol{\varepsilon}}^p + \frac{1}{2} \boldsymbol{\sigma} : \dot{\mathbf{C}} : \boldsymbol{\sigma} \right) \frac{1}{g_f} = 0. \tag{A.4}$$

Inserting Eq. (6):

$$\boldsymbol{\Lambda} : \left(\mathbf{D} : (\dot{\boldsymbol{\varepsilon}} - \dot{\boldsymbol{\varepsilon}}^p - \dot{\mathbf{C}} : \boldsymbol{\sigma}) \right) - \frac{\partial \mathcal{K}}{\partial \kappa^{pd}} \left(\boldsymbol{\sigma} : \dot{\boldsymbol{\varepsilon}}^p + \frac{1}{2} \boldsymbol{\sigma} : \dot{\mathbf{C}} : \boldsymbol{\sigma} \right) \frac{1}{g_f} = 0 \tag{A.5}$$

Substituting Eqs. (12) and (11) and rearranging leads to

$$\begin{aligned} \boldsymbol{\Lambda} : \mathbf{D} : \dot{\boldsymbol{\varepsilon}}^p - \dot{\lambda} (& \boldsymbol{\Lambda} : \mathbf{D} : \boldsymbol{\Lambda} (1 - \xi) + \xi \boldsymbol{\Lambda} : \mathbf{D} : \frac{\boldsymbol{\Lambda} \otimes \boldsymbol{\Lambda}}{\boldsymbol{\Lambda} : \boldsymbol{\sigma}} : \boldsymbol{\sigma} \\ & + (1 - \xi) \frac{\partial \mathcal{K}}{\partial \kappa^{pd}} \boldsymbol{\sigma} : \boldsymbol{\Lambda} \frac{1}{g_f} + \frac{\xi}{2 g_f} \frac{\partial \mathcal{K}}{\partial \kappa^{pd}} \boldsymbol{\sigma} : \frac{\boldsymbol{\Lambda} \otimes \boldsymbol{\Lambda}}{\boldsymbol{\Lambda} : \boldsymbol{\sigma}} : \boldsymbol{\sigma}) = 0, \end{aligned} \tag{A.6}$$

which can be rewritten as

$$\dot{\lambda} = \frac{\boldsymbol{\Lambda} : \mathbf{D} : \dot{\boldsymbol{\varepsilon}}}{A + B + C + D} \tag{A.7}$$

being

$$A = (1 - \xi) \boldsymbol{\Lambda} : \mathbf{D} : \boldsymbol{\Lambda} \tag{A.8a}$$

$$B = (1 - \xi) \frac{\partial \mathcal{K}}{\partial \kappa^{pd}} \boldsymbol{\sigma} : \boldsymbol{\Lambda} / g_f \tag{A.8b}$$

$$C = \xi \boldsymbol{\Lambda} : \mathbf{D} : \frac{\boldsymbol{\Lambda} \otimes \boldsymbol{\Lambda}}{\boldsymbol{\Lambda} : \boldsymbol{\sigma}} : \boldsymbol{\sigma} \tag{A.8c}$$

$$D = \frac{\xi}{2 g_f} \frac{\partial \mathcal{K}}{\partial \kappa^{pd}} \boldsymbol{\sigma} : \frac{\boldsymbol{\Lambda} \otimes \boldsymbol{\Lambda}}{\boldsymbol{\Lambda} : \boldsymbol{\sigma}} : \boldsymbol{\sigma} \tag{A.8d}$$

Appendix B. Derivation of the analytical tangent tensor

The tangent constitutive tensor is the one that relates the strain temporal increment with its corresponding stress increment, i.e.

$$\dot{\boldsymbol{\sigma}} = \mathbf{D}^t : \dot{\boldsymbol{\varepsilon}}. \tag{B.1}$$

Developing the strain term:

$$\dot{\boldsymbol{\sigma}} = \mathbf{D} : (\dot{\boldsymbol{\varepsilon}} - \dot{\boldsymbol{\varepsilon}}^p - \dot{\mathbf{C}} : \boldsymbol{\sigma}) = \mathbf{D} : \dot{\boldsymbol{\varepsilon}} - \mathbf{D} : \dot{\boldsymbol{\varepsilon}}^p - \mathbf{D} : \dot{\mathbf{C}} : \boldsymbol{\sigma} \tag{B.2}$$

and substituting with Eqs. (11) and (12) yields

$$\dot{\boldsymbol{\sigma}} = \mathbf{D} : \dot{\boldsymbol{\varepsilon}} - \mathbf{D} : (1 - \xi) \dot{\lambda} \boldsymbol{\Lambda} - \mathbf{D} : \xi \, \dot{\lambda} \, \frac{\boldsymbol{\Lambda} \otimes \boldsymbol{\Lambda}}{\boldsymbol{\Lambda} : \boldsymbol{\sigma}} \tag{B.3}$$

and substituting the plastic multiplier $\dot{\lambda}$ with Eq. (18) and rearranging:

$$\dot{\boldsymbol{\sigma}} = \mathbf{D} : \dot{\boldsymbol{\varepsilon}} - \left[\mathbf{D} : (1 - \xi) \boldsymbol{\Lambda} - \mathbf{D} : \xi \, \frac{\boldsymbol{\Lambda} \otimes \boldsymbol{\Lambda}}{\boldsymbol{\Lambda} : \boldsymbol{\sigma}} \right] \frac{\boldsymbol{\Lambda} : \mathbf{D} : \dot{\boldsymbol{\varepsilon}}}{A + B + C + D} \tag{B.4}$$

which after some manipulation, one can state that the tangent tensor is expressed as

$$\mathbf{D}^t = \mathbf{D} - \frac{\left[(1 - \xi) \mathbf{D} : \boldsymbol{\Lambda} + \xi \mathbf{D} : \frac{\boldsymbol{\Lambda} \otimes \boldsymbol{\Lambda}}{\boldsymbol{\Lambda} : \boldsymbol{\sigma}} : \boldsymbol{\sigma} \right] \otimes [\boldsymbol{\Lambda} : \mathbf{D}]}{A + B + C + D}. \tag{B.5}$$

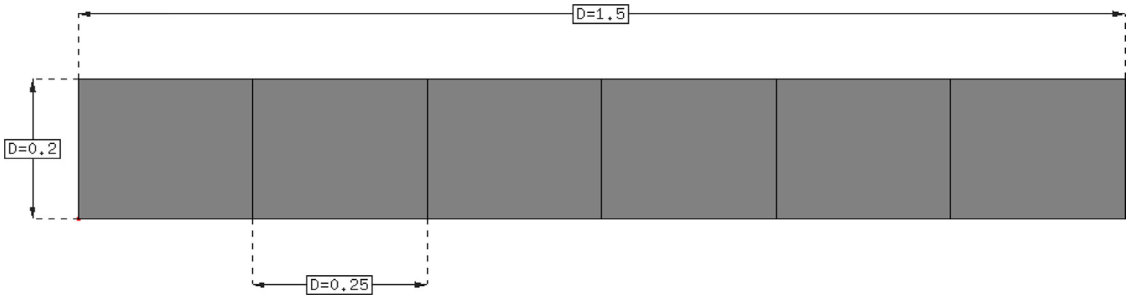

Fig. C.23. Geometry used for testing the convergence rate of the model.

Appendix C. Convergence rate study of the implemented model

In order to achieve quadratic convergence rate in the Newton–Raphson strategy, a good estimation of the linearized tangent constitutive tensor has to be employed. Eq. (21) defines mathematically the analytical linearization of the plastic-damage model, this is one of the approaches that can be used.

For general purposes, especially when the analytical derivation is not possible (composite materials, non-associative plasticity, etc.), one can obtain a good estimation of the tangent constitutive matrix by means of a numerical approach, also called as perturbation method [39,40]. This solution is based on approximating the derivatives in Eq. (20) via different finite differences schemes.

A first order approximation consists in performing a forward Euler scheme as:

$$\mathbf{D}^t_j \simeq \frac{\boldsymbol{\sigma}(\boldsymbol{\varepsilon} + \boldsymbol{\delta\varepsilon}_j) - \boldsymbol{\sigma}(\boldsymbol{\varepsilon})}{\delta\varepsilon_j} \tag{C.1}$$

where $\mathbf{D}^t_j$ is the jth column of the tangent constitutive tensor and $\boldsymbol{\delta\varepsilon}_j$ is a zero vector except for the jth component whose value is a strain perturbation $\delta\varepsilon_j$, $\boldsymbol{\sigma}$ and $\boldsymbol{\varepsilon}$ are measures of stresses and strains, respectively.

A more exact approach but also more computationally expensive consists in using a central differences scheme, i.e.

$$\mathbf{D}^t_j \simeq \frac{\boldsymbol{\sigma}(\boldsymbol{\varepsilon} + \boldsymbol{\delta\varepsilon}_j) - \boldsymbol{\sigma}(\boldsymbol{\varepsilon} - \boldsymbol{\delta\varepsilon}_j)}{2\delta\varepsilon_j}. \tag{C.2}$$

The central differences approach improves the convergence rate with respect to the standard forward Euler scheme. However, applying a perturbation backwards ($\boldsymbol{\varepsilon} - \boldsymbol{\delta\varepsilon}_j$) implies an unloading condition for the constitutive law, which is not the expected behaviour of the finite difference scheme.

In order to circumvent this issue and provide a fully consistent finite differences scheme, a novel approach is proposed that consists in performing a forward Euler method taking also into account the second order terms, which after some mathematical manipulation is expressed as:

$$\mathbf{D}^t_j \simeq \frac{\boldsymbol{\sigma}(\boldsymbol{\varepsilon} + \boldsymbol{\delta\varepsilon}_j) - \boldsymbol{\sigma}(\boldsymbol{\varepsilon})}{\delta\varepsilon_j} - \frac{\boldsymbol{\sigma}(\boldsymbol{\varepsilon} + 2\boldsymbol{\delta\varepsilon}_j) - 2\boldsymbol{\sigma}(\boldsymbol{\varepsilon} + \boldsymbol{\delta\varepsilon}_j) + \boldsymbol{\sigma}(\boldsymbol{\varepsilon})}{2\delta\varepsilon_j}. \tag{C.3}$$

With the objective of assessing the convergence rate of the previous tangent approximations, a benchmark numerical example is proposed. The geometry of the sample is depicted in Fig. C.23. The left end if fully fixed whereas on the right end a monotonic increasing horizontal displacement is imposed.

Fig. C.24 shows the ratio of the residual error in logarithmic scale for the different tangent tensor estimations. As expected, the numerical approximations of the tangent tensor converge quadratically, being the second order solutions slightly better than the forward Euler approximation.

Appendix D. Yield surfaces used

Since most of the yield surfaces exposed are formulated in terms of the stress invariants, a brief description of them and the so-called Lode's angle is given below. Also, all the yield surfaces described in this work follow the same structure:

$$\mathcal{F} = f(\boldsymbol{\sigma}) - \mathcal{K} \tag{D.1}$$

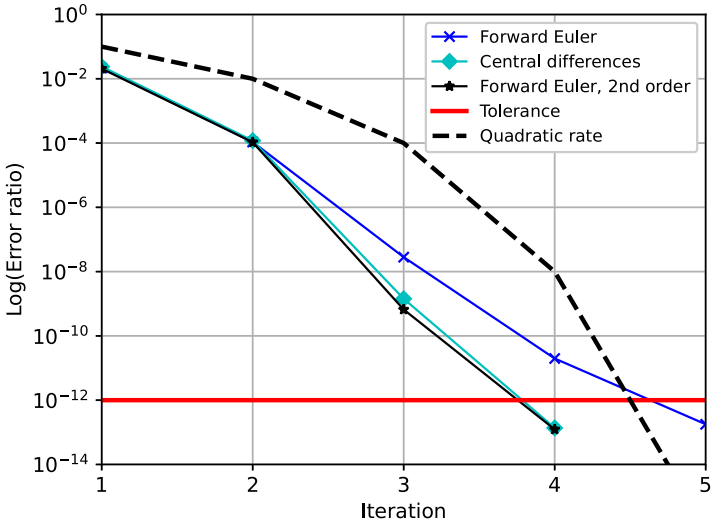

Fig. C.24. Convergence rate for different tangent tensor approximations.

where $\mathcal{F}$ defines the elastic domain (when lower than zero), $f(\boldsymbol{\sigma})$ is the uniaxial stress measure and $\mathcal{K}$ is the material threshold.

D.1. Stress invariants and other computations

D.1.1. Stress invariants

$$\mathrm{I}_1 = \sigma_{11} + \sigma_{22} + \sigma_{33} = \mathrm{tr}(\boldsymbol{\sigma}) \tag{D.2}$$

$$\mathrm{I}_2 = \sigma_{11}\sigma_{22} + \sigma_{22}\sigma_{33} + \sigma_{11}\sigma_{33} - \sigma_{12}^2 - \sigma_{23}^2 - \sigma_{31}^2 \tag{D.3}$$

$$\mathrm{I}_3 = \det(\boldsymbol{\sigma}) \tag{D.4}$$

D.1.2. Stress deviator invariants

The stress deviatoric tensor s_{ij} is defined as:

$$\mathbf{s} = \boldsymbol{\sigma} - \frac{\mathrm{I}_1}{3}\mathbf{I} \tag{D.5}$$

where I_1 is the first stress invariant (Eq. (D.2)) and $\mathbf{I}$ the identity tensor. Based on the deviatoric stress tensor, the following invariants can be defined:

$$\mathrm{J}_1 = 0 \tag{D.6}$$

$$\mathrm{J}_2 = \frac{1}{3}\mathrm{I}_1^2 - \mathrm{I}_2 \tag{D.7}$$

$$\mathrm{J}_3 = \frac{2}{27}\mathrm{I}_1^3 - \frac{1}{3}\mathrm{I}_1\mathrm{I}_2 + \mathrm{I}_3 \tag{D.8}$$

D.1.3. Lode's angle θ

Geometrically, the Lode Angle is the smallest angle between the line of pure shear and the projection of the stress tensor on the deviatoric plane. The mathematical expression is:

$$\theta = \frac{1}{3}\mathrm{asin}\left(\frac{-3\sqrt{3}\mathrm{J}_3}{2\mathrm{J}_2\sqrt{\mathrm{J}_2}}\right) \tag{D.9}$$

D.2. Circumscribed Drucker–Prager yield surface

This criterion formulated by Drucker and Prager in 1952 is considered as a smoothed approximation to the Mohr–Coulomb criterion. However, the mathematical formulation arises from a generalization of the Von Mises criterion to include the influence of pressure, through the first invariant of the stress tensor I_1 and the internal friction angle ϕ.

Uniaxial stress

$$f(\boldsymbol{\sigma}) = \left(\frac{-\sqrt{3}(3-\sin\phi)}{3\sin\phi - 3}\right)\left(\frac{2\mathrm{I}_1\sin\phi}{\sqrt{3}(3-\sin\phi)} + \sqrt{\mathrm{J}_2}\right) \tag{D.10}$$

Material threshold

$$\mathcal{K} = f_t\left(\frac{3+\sin\phi}{3\sin\phi - 3}\right) \tag{D.11}$$

Being f_t the yield stress.

D.3. Huber-Von-Mises yield surface

This criterion was formulated by Von Mises in 1913, and like the two former, depends only on one single parameter, the maximum octahedral shear strength τ_{oct}^{max}. Moreover, it only considers the second invariant of the stress deviatoric tensor J_2, neglecting hence the influence of the first invariant of the stress tensor I_1 and the third invariant of the stress deviatoric tensor J_3.

Uniaxial stress

$$f(\boldsymbol{\sigma}) = \sqrt{3\mathrm{J}_2} \tag{D.12}$$

Material threshold

$$\mathcal{K} = f_t \tag{D.13}$$

D.4. Modified Mohr–Coulomb yield surface

The use of the original Mohr–Coulomb yield criterion for materials of the concrete type, has the disadvantage of not fulfilling the relationship between the uniaxial tensile and compressive strength for friction angles ϕ usually employed for concrete ($\phi \approx 30 - 35\,deg$).

Among the solutions usually adopted to overcome the problem is to increase this internal friction angle ϕ until the required initial uniaxial resistance ratio is reached. However, this is not a valid solution when working with associative plasticity, since the Mohr–Coulomb criterion defined as a surface of plastic potential with a dilatancy angle $\psi = \phi$, would produce in the solid an excessive effect of the dilatancy phenomenon.

In order to be able to operate with associative plasticity, and to avoid the drawback of using the Mohr–Coulomb function defined with a very high internal friction angle, a simple modification of the original criterion mentioned above is proposed in Oller et al. [9] is proposed as:

Uniaxial stress

$$f(\boldsymbol{\sigma}) = \frac{2\tan(\pi/4+\phi/2)}{\cos\phi}\left(\frac{\mathrm{I}_1\mathbb{K}_3}{3} + \sqrt{\mathrm{J}_2}\left(\mathbb{K}_1\cos\theta - \frac{\mathbb{K}_2\sin\theta\sin\phi}{\sqrt{3}}\right)\right) \tag{D.14}$$

being:

$$\mathbb{K}_1 = 0.5(1+\alpha_r) - 0.5(1-\alpha_r)\sin\phi \tag{D.15a}$$

$$\mathbb{K}_2 = 0.5(1+\alpha_r) - 0.5(1-\alpha_r)/\sin\phi \tag{D.15b}$$

$$\mathbb{K}_3 = 0.5(1+\alpha_r)\sin\phi - 0.5(1-\alpha_r) \tag{D.15c}$$

$$\alpha_r = \frac{f_c/f_t}{\tan\left(\pi/4 + \phi/2\right)^2} \tag{D.15d}$$

Material threshold

$$\mathcal{K} = f_c \quad \text{(yield stress in compression)} \tag{D.16}$$

D.5. Rankine yield surface

This criterion was formulated by Rankine in 1876 and is based on one single parameter, the maximum uni-axial tension strength f_t. Additionally, it is influenced by the first invariant of the stress tensor I_1 and by the second and third invariants of the deviatoric stress tensor J_2, J_3, respectively. This criterion helps to set in the limits in a simple way where the fracturing process starts in a point of a solid. This hypothesis leads to the assumption that fractures occur when the maximum main stress reaches the value of the uni-axial tension strength f_t.

Uniaxial stress

$$f(\boldsymbol{\sigma}) = \max(\sigma_I, \sigma_{II}, \sigma_{III}) \tag{D.17}$$

As a function of the invariants of the stress tensor and its deviatoric stress tensors:

$$f(I_1, J_2, \theta, f_t) = 2\sqrt{3J_2}\cos(\theta + \pi/6) + I_1 - 3f_t = 0 \tag{D.18}$$

Material threshold

$$\mathcal{K} = f_t \tag{D.19}$$

References

[1] M. Cervera, G. Barbat, M. Chiumenti, Architecture of a multi-crack model with full closing, reopening and sliding capabilities, Comput. Mech. (6) (2020) 1593–1620.

[2] L.M. Kachanov, Introduction to damage mechanics, in: Mechanics of Elastic Stability, Martinus Nijhoff Publishers, 1986.

[3] J.L. Chaboche, Continuum damage mechanics: Part I-General concepts, J. Appl. Mech. (55) (1988) 59–64.

[4] J.L. Chaboche, Continuum damage mechanics: Part II-damage growth, crack initiation, crack growth, J. Appl. Mech. (55) (1988) 65–72.

[5] J. Mazars, J. Lemaitre, Application of continuous damage mechanics to strain and fracture behavior of concrete, Appl. Fract. Mech. Cem. Compos. (1985) 507–520.

[6] J. Oliver, M. Cervera, S. Oller, J. Lubliner, Isotropic damage models and smeared crack analysis of concrete, in: Second International Conference on Computer Aided Analysis and Design of Concrete Structures, 1990.

[7] J.C. Simo, J.W. Ju, Strain and stress based based continuum damage models I. Formulation, Int. J. Solids Struct. (23) (1987) 821–840.

[8] J.C. Simo, J.W. Ju, Strain and stress based based continuum damage models II. Computational aspects, Int. J. Solids Struct. (23) (1987) 841–869.

[9] S. Oller, E. Oñate, J. Oliver, J. Lubliner, Finite element nonlinear analysis of concrete structures using a plastic-damage model, Eng. Fract. Mech. (35) (1990) 219–231.

[10] B. Luccioni, S. Oller, R. Danesi, Coupled plastic-damaged model, Comput. Methods Appl. Mech. Engrg. (129) (1996) 81–89.

[11] M. Poliotti, J.M. Bairán, A new concrete plastic-damage model with an evolutive dilatancy parameter, Eng. Struct. (189) (2019) 541–549.

[12] J. Lubliner, J. Oliver, S. Oller, E. Oñate, A plastic-damage model for concrete, Int. J. Solids Struct. (25) (1989) 299–326.

[13] G. Meschke, R. Lackner, H.A. Mang, An anisotropic elastoplastic-damage model for plain concrete, Int. J. Numer. Methods Eng. (42) (1998) 703–727.

[14] J.Y. Wu, M. Cervera, A thermodynamically consistent plastic-damage framework for localized failure in quasi-brittle solids: Material model and strain localization analysis, Int. J. Solids Struct. (88–89) (2016) 227–247.

[15] S. Oller, Nonlinear Dynamics of Structures, CIMNE-Springer, ISBN: 978-3-319-05193-2, 2014.

[16] J.C. Simo, J. Oliver, F. Armero, An analysis of strong discontinuities induced by stress-softening in rate-independent inelastic solids, Comput. Mech. (12) (1993) 277–296.

[17] S. Govindjee, G.J. Kay, J.C. Simo, Anisotropic modelling and numerical simulation of brittle damage in concrete, Int. J. Numer. Methods Eng. (38) (1995) 3611–3634.
[18] A. Cornejo, L.G. Barbu, C. Escudero, X. Martínez, S. Oller, A.H. Barbat, Methodology for the analysis of post-tensioned structures using a constitutive serial-parallel rule of mixtures, Compos. Struct. (200) (2018) 480–497.
[19] A. Cornejo, L.G. Barbu, X. Martínez, S. Oller, A.H. Barbat, Methodology for the analysis of post-tensioned structures using a constitutive serial-parallel rule of mixtures: Large scale non-linear analysis, Compos. Struct. (216) (2019) 315–330.
[20] S. Jiménez, A. Cornejo, L.G. Barbu, S. Oller, A.H. Barbat, Analysis of the mock-up of a reactor containment building: Comparison with experimental results, Nucl. Eng. Des. (359) (2020) 110454.
[21] S. Jiménez, A. Cornejo, L.G. Barbu, A.H. Barbat, S. Oller, Failure pressure analysis of a nuclear reactor prestressed concrete containment building, Eng. Struct. (236) (2021) 112052.
[22] J. Lee, G.L. Fenves, Plastic-damage model for cyclic loading of concrete structures, J. Eng. Mech. ASCE (1998).
[23] J. Lee, G.L. Fenves, Pa plastic-damage concrete model for earthquake analysis of dams, Earthq. Eng. Struct. Dyn. (27) (1998) 937–956.
[24] F. Armero, S. Oller, A general framework for continuum damage models. I: Infinitesimal plastic damage models in stress space, Int. J. Solids Struct. (37) (2000) 7409–7464.
[25] E. Oñate, S. Oller, J. Oliver, J. Lubliner, A constitutive model for cracking of concrete based on the incremental theory of plasticity, Eng. Comput. (5) (1988) 309–319.
[26] J.Y. Wu, J. Li, R. Faria, An energy release rate-based plastic-damage model for concrete, Int. J. Solids Struct. (43) (2004) 583–612.
[27] S. Oller, Un Modelo de Daño Continuo Para Materiales-Friccionales (Ph.D. thesis), Universitat Politècnica de Catalunya, 1988.
[28] P. Davvand, R. Rossi, E, Oñate an object-oriented environment for developing finite element codes for multi-disciplinary applications, Arch. Comput. Methods Eng. (17) (2010) 253–297.
[29] P. Davvand, R. Rossi, M. Gil, X. Martorell, J. Cotela, E. Juanpere, S. Idelsohn, E. Oñate, Migration of a generic multi-physics framework to HPC environments, Comput. Fluids (80) (2013) 301–309.
[30] D. Karsan, J.O. Jirsa, Behavior of concrete under compressive loadings, J. Struct. Div. (95) (1969) 2543–2564.
[31] PhC. Perdikaris, A. Romeo, Size effect in fracture energy of concrete and stability issues in three-point bending fracture toughness testing, ACI Mater. (92) (1995) 483–496.
[32] E. Osorio, J.M. Bairán, A. Marí, Lateral behavior of concrete under uniaxial compressive cyclic loading, Mater. Struct. (46) (2013) 709–724.
[33] V. Garcia-Alvarez, R. Gettu, I. Carol, Analysis of mixed-mode fracture in concrete using interface elements and a cohesive crack model, Sādhanā (37) (2012) 187–205.
[34] G. Barbat, et al., Structural size effect: Experimental, theoretical and accurate computational assessment, Eng. Struct. (213) (2020) 110555.
[35] A. Cornejo, A Fully Lagrangian Formulation for Fluid–Structure Interaction Between Free-Surface Flows and Multi-Fracturing Solids (Ph.D. thesis), Universitat Politècnica de Catalunya, 2021.
[36] B. Bourdin, G. Francfort, J.-J. Marigo, Numerical experiments in revisited brittle fracture, J. Mech. Phys. Solids (48–4) (2000) 797–826.
[37] C. Miehe, M. Hofacker, F. Welschinger, A phase field model for rate-independent crack propagation: robust algorithmic implementation based on operator splits, Comput. Methods Appl. Mech. Engrg. (199) (2010) 2765–2778.
[38] J.-Y. Wu, V. Nguyen, A length scale insensitive phase-field damage model for brittle fracture, J. Mech. Phys. Solids (119) (2018) 20–42.
[39] A. Cornejo, V. Mataix, F. Zárate, E. Oñate, Combination of an adaptive remeshing technique with a coupled FEM-DEM approach for analysis of crack propagation problems, Comput. Part. Mech. (2019) 1–18.
[40] A. Cornejo, A. Franci, F. Zárate, E. Oñate, A fully Lagrangian formulation for fluid–structure interaction problems with free-surface flows and fracturing solids, Comput. Struct. (250) (2021) 106532.